HYBRID SURFACE PLASMON DAMPING

CHEMICAL SENSOR

By

SRIHARSHA KARUMURI

Bachelor of Engineering in Mechanical Engineering

Andhra University

Visakhapatnam, Andhra Pradesh, INDIA

2006

Submitted to the Faculty of the
Graduate College of the
Oklahoma State University
in partial fulfillment of
the requirements for
the Degree of
MASTER OF SCIENCE
May, 2009

HYBRID SURFACE PLASMON DAMPING

CHEMICAL SENSOR

Thesis Approved:

Dr. A. Kaan Kalkan
Assistant Professor in Mechanical and Aerospace Engineering
Thesis Advisor

Dr. Raman P. Singh
Associate Professor in Mechanical and Aerospace Engineering
Committee Member

Dr. Barry K. Lavine
Associate Professor in Chemistry
Committee Member

Dr. A. Gordon Emslie
Professor in Physics and Dean of the Graduate College

Acknowledgements

My first and foremost thanks to Dr. A Kaan Kalkan for rendering me support in every step of my research work from choosing the topic to presenting the work. I am indebted to him for the concepts he taught me on Nanotechnology, Materials Science and Physics, and also for providing his constant support, training, guidance and patience throughout my Masters Thesis work. I would also like to thank Dr Raman P Singh and Dr Barry K Lavine for investing their valuable time in giving helpful feedback on present work.

I express my thanks to Dr. Murat Yasar of Techno-Sciences, Inc., MD for providing us with software for fitting Lorentzian curves. I also appreciate Dr Subhendu Guha of United Solar, Inc., Auburn Hills MI, for silicon substrates. Also, I want to convey my acknowledgements to Dr Susheng Tan of Oklahoma State University Microscopy Laboratory and Mr. Karthik Bhatt for TEM and AFM micrographs. Finally, I owe my thanks to all the members of Functional Nanomaterials Laboratory for giving me support and encouragement.

I would like to express my gratitude to Oklahoma State Regents for Higher Education (OSRHE), Oklahoma State University and U.S. Air force for sponsoring the project. I am also grateful to my parents, sister and friends for their support and motivation.

TABLE OF CONTENTS

LIST OF FIGURES

Chapter.1

Introduction

Since the medieval centuries, noble metal nanoparticles have provided the unfading brilliant colors in stained glass windows, pottery, and paintings. It was not until Gustav Mie (1908), however, these beautiful colors were attributed to the resonant coupling of light with the collective electron oscillations of nanoparticles, namely the localized surface plasmon modes [1-14]. This fascinating phenomenon, that is the resonant coupling of light with localized surface plasmons, is subject to spectral shifts when the nanoparticles undergo electromagnetic or charge interactions with their environment. Such spectral shifts are easily detectable by conventional spectrometers,

and at times with the naked eye. As a result, localized surface plasmon resonance (LSPR) opens the door to the development of a new generation of chemical sensors.

In particular, with the launch of intense research activity in the fabrication and utilization of nanostructures in recent years, localized surface plasmon resonance sensors have gained significant attention with the objective of detecting biomolecules, explosives, toxins, and warfare agents at trace levels [2-14]. Up to present, all LSPR sensing demonstrations exploited the frequency and intensity shift of the LSPR optical extinction peak due to the variation in: 1) polarizability (i.e., refractive index) of the medium surrounding the metal nanoparticle; and, 2) charge transfer to / from the metal nanoparticle [2-14].

On the other hand, the present thesis work brings into play a third impetus that will induce a change in LSPR. This is the increase in damping of the hybrid plasmon mode due to atomic/molecular adsorption at the surface of the nanoparticle. Hybrid plasmon modes develop when strong electromagnetic coupling between adjacent nanoparticles occur. "Plasmon hybridization" may be interpreted as interference or superposition of regular plasmon modes (modes seen for isolated particles) [1, 15-17].

In a nutshell, the concept of plasmon damping may be explained using an oscillator model, where a spring-mass system is resonantly excited with a harmonically acting force. The harmonic force represents the electromagnetic field (light). The natural frequency of the system corresponds to the plasmon frequency. Furthermore, the viscous friction of the system is analogous to the electron scattering at the nanoparticle surface. The increase of the viscous dissipation will amount to reduced amplitude of the oscillation. In the nanoparticle, this happens when a molecule adsorbs on the

nanoparticle surface and increases the electron scattering. The consequence is reduction in optical density of the plasmon mode. This is measured as a reduction in optical extinction. Accordingly, the present work employs the damping of plasmon modes as a probe to detect adsorbates on the nanoparticle surface. More specifically, in the present thesis work, these are the hybrid plasmon modes. It is found out in the present effort that this novel sensing mechanism offers superior sensitivity over conventional LSPR sensing approaches.

In addition to the aforementioned novel sensing mechanism (i.e., hybrid plasmon damping), the sensor development effort in the present thesis employs a unique nanofabrication technique: "electroless reduction of metal nanoparticles on silicon". This novel technique enables the fabrication of monolayer of surfactant-free, size-controlled metal nanoparticles on silicon [18]. The metal nanoparticle synthesis is as quick and easy as immersion of silicon films in a metal salt solution for several seconds. During the synthesis, the interparticle separation is observed to shrink to as low as a few nanometers, but the particles never impinge each other. As a result, strong and well-resolved hybrid plasmon modes develop enhancing the sensitivity. This has been attributed to the unique "nanometal on semiconductor" approach, wherein the charge transfer between the metal nanoparticles and silicon film gives rise to Coulombic repulsion between the particles. As will be evident in the following chapters, the unique nanofabrication approach and sensing mechanism of the present effort are critical to the outstanding sensor performance demonstrated. A further innovative step achieved during the course of the present work is the dramatic reduction of intrinsic hybrid plasmon damping by annealing of the nanoparticle monolayers synthesized on silicon. The minimization of intrinsic plasmon

damping provides a substantial enhancement in sensitivity. Once the intrinsic damping is minimized, damping due to molecular adsorption on the nanoparticle causes a more significant fractional change in total damping.

LSPR sensors typically make use of gold and silver nanoparticles due to the occurrence of LSPR in the visible region of electromagnetic spectrum in these metals [1-14]. Among all metals, silver exhibits the strongest LSPR due to its lowest plasmon damping. As will be detailed in the following chapters, the present thesis work employs silver nanoparticles. In typical surface plasmon resonance sensing applications, the nanoparticles are functionalized with specific molecules, which have high affinity to the chemical agent to be detected. In a LSPR biosensor targeting prostate cancer antigen, for example, the nanoparticles must be functionalized with specific antibodies recognizing the antigen [8, 9]. In other words, those antibodies have the highest affinity to the prostate cancer antigens. Similarly, the hybrid plasmon damping sensor of the present thesis work can be made specific to a myriad of agents by decoration of the nanoparticles with specific receptor molecules. However, for the sake of simplicity, the initial investigation here is directed towards detection of mercury in air. Fortunately, silver already has very high affinity for mercury, and hence the nanoparticle surfaces need not be functionalized with any receptor molecules. Strong interaction of mercury with silver is expected to distort the local electric potential at the metal surface leading to increased electron scattering. In case the intrinsic scattering is minimal, this additional scattering will have a prominent impact on damping of the LSPR. In fact, this is the sensing mechanism employed in the present effort.

In addition to being an ideal testing agent for the novel sensor of the present effort, mercury is also a severe neurotoxin, whose detection and quantification in the environment is of utmost importance. Due to rapid industrialization and growing utilization of fossil fuels, not only the concentration of green houses gases but also certain toxins in the atmosphere has increased. Mercury vapor and hydrogen sulfide are two of such toxins in atmosphere whose concentration has surpassed the natural level due to industrialization. In particular, the average mercury level in the environment has tripled since the beginning of the industrial revolution. According to toxicologists, mercury can be adverse when its level in blood is beyond 200 ppb and in hair beyond 50 ppm [19]. In 1950 Minamata Bay, Japan, many children were affected with mental retardation, disturbances in gait, speech, and swallowing, as well as abnormal reflexes due to mercury contamination [20]. According to the statistics of Unites States Center for Disease control and Prevention (CDC), every 1 pregnant woman out of 10 has enough mercury in her blood to cause damage to the fetus [20]. Mercury not only damages the brain but also the liver, kidneys, and the spinal cord.

Mercury ions are easily converted to methyl mercury by methanogenic bacterium, anaerobes, and aerobes. Methyl mercury is considered as the most toxic form of mercury which can easily bind to fish protein and other aquatic animals, which ultimately transforms aquatic food toxic to eat [21]. Elemental mercury in the atmosphere infects the water bodies due to rain and ran off. The main source of mercury contamination in the atmosphere is coal based power plants, and combustion of fossil fuels. In addition, mercury is released from chloralkali plants, dentistry and pesticide industries. Therefore, there is an urgent need for the development of low-cost, hand-held, high-sensitivity

mercury detection devices in industries and thermal power plants to monitor the mercury levels released to the environment. Accordingly, the research effort of the present thesis for the development of the nanoparticle based hybrid plasmon damping sensor is partially motivated by this need.

The organization of the present thesis is as follows. Chapter 2 presents a detailed quantitative review on LSPR and conventional LSPR sensing mechanisms. It also provides the essential background in plasmon hybridization. In Chapter 3, the procedures for nanoparticle synthesis, minimization of hybrid plasmon damping, and measurement of plasmon extinction in response to mercury vapor exposures are described. Chapter 4 presents the results. In particular, kinetics of hybrid plasmon extinction in response to mercury vapor in air, nitrogen and argon is given. These optical extinction spectra are analyzed computationally to quantify the kinetics of plasmon damping and thereby the number of mercury adsorbates on silver nanoparticles. Also in this chapter, adsorption kinetics is discussed in view of the Langmuir adsorption equation, and adsorbate-induced hybrid plasmon damping is interpreted in terms of electron scattering and chemical interface damping. Finally, in Chapter 5, conclusions are drawn as well as future research directions are suggested.

Chapter.2

Review of Literature and Background

The present Chapter is dedicated to the introduction of various concepts, which are instrumental in the development of the novel “hybrid plasmon damping sensing technology” described. The Chapter starts with the explanation of localized surface plasmon resonance (LSPR) on the basis of a simple force-constant and damper model. Subsequently, LSPR is also elucidated in the framework of electromagnetism and Mie Equation. Meanwhile, concepts of scattering, absorption, extinction, and extinction cross section are elucidated. In particular, the Author derives a mathematical expression relating the plasmon extinction to total number of electrons contributing to plasmon and plasmon damping constant. This mathematical expression underlies the novel scheme of

sensing in the present thesis. Finally, the chapter completes with the description of plasmon hybridization and hybrid plasmon modes.

2.1 Localized surface plasmon resonance sensor (LSPR); Analogy with a spring mass system

Classically, the "localized plasmon" in a metal nanoparticle can be treated as a mass of electrons M, moving coherently (all in phase) under the action of an oscillating electric field (i.e., electromagnetic radiation). In an isolated nanoparticle, these electrons oscillating in phase are the conduction (i.e., valence) electrons. Taking the convenience of free electron theory of metals, one can split the nanoparticle into two components: 1) conduction electrons of total mass M, and total charge $-Q$; 2) positive atomic cores of total charge Q. Each conduction electron is equally shared by the atomic cores and delocalized in the nanoparticle. At the same time, however, the overall mass of conduction electrons is bound to the atomic cores by Coulombic attraction (attraction between Q and $-Q$). As a first approximation, this restoring force, F_r, can be described by $F_r = -kx$, k being the effective force constant and x being the displacement of the center of mass/charge of the conduction electron mass from its equilibrium position. Hence, LSPR is analogous to a spring-mass system as illustrated in Figure 2.1, where the resonant angular frequency is simply given by $\omega_o = \sqrt{k/M}$.

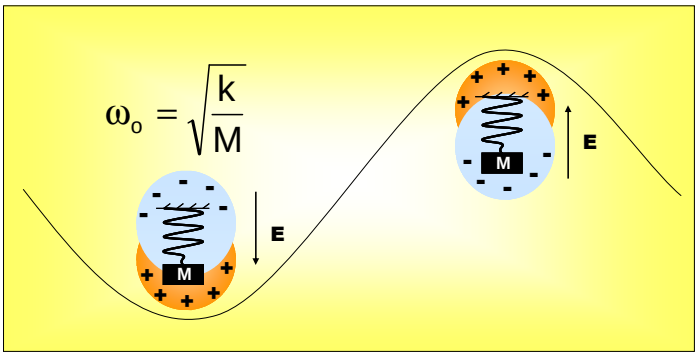

Figure 2.1: Spring- mass analogy to LSPR [1-14].

In a true physical system, one should also take into consideration the damping factor. Accordingly, the equation of motion for the plasmon is given by

$$M\ddot{x} = -kx - M\Gamma\dot{x} - QEe^{i\omega t} \tag{2.1}$$

where E and ω are the amplitude and angular frequency of the oscillating electric field, while t denotes the time. Here, Γ is the phenomenological damping constant per electron that takes into account the scattering (i.e., electron-phonon, electron-electron, electron-defect and electron-surface scattering). In the language of classical mechanics, $M\Gamma\dot{x}$ is the viscous force experienced by the conduction electron mass. Equation 2.1 can be rearranged to:

$$\ddot{x} + \Gamma\dot{x} + \omega_0{}^2 x = -\frac{eE}{m_e} e^{i\omega t} \tag{2.2}$$

where e and m_e are the electron charge and mass, respectively. Equation 2.2 can be solved by substituting $x = Xe^{i\omega t}$ as

$$x = \frac{(-e/m_e)Ee^{i\omega t}}{(\omega_0{}^2 - \omega^2) + i\omega\Gamma} \tag{2.3}$$

Obviously, x undergoes a resonance at $\omega = \omega_o$ (denominator minimizes) suggesting the origin of localized surface plasmon resonance observed in metal nanoparticles. This resonance simply reveals itself in terms of color. Color formation results from nanoparticles absorbing or scattering light strongly at a certain range of the electromagnetic spectrum centered around $\omega = \omega_o$. For example, gold and silver nanospheres of 20 nm diameter exhibit a strong absorption at green and blue, respectively. As a result, upon illumination, the transmitted light looks red and brown, respectively. The resonance spectrum can be obtained by measurement of the optical transmission as a function of wavelength/frequency. In other words, from optical transmission, one can derive how much power the nanoparticles "steal" from the impingent electromagnetic field. Theoretically, the power extracted from the field by a single nanoparticle is the time rate of work done by the electric field on the plasmon. The time-averaged extracted power $P_{excitation}$ also equals the time-averaged power dissipated by the nanoparticle, $P_{excitation}$ considering steady state conditions. In summary,

$$P_{excitation} = \left\langle \dot{x}(-QEe^{i\omega t}) \right\rangle = P_{extinction} = \left\langle \dot{x}(M\Gamma\dot{x}) \right\rangle \qquad (2.4)$$

where the brackets indicate time-averaged values. Substituting for x from Equation 2.3, $P_{excitation}$ is given by

$$P_{extinction} = \left(\frac{E^2 e}{2m_e} \right) \frac{\omega^2 \Gamma Q}{(\omega^2 - \omega_o{}^2)^2 + \omega^2 \Gamma^2} \qquad (2.5)$$

In quantum mechanical terms, when a photon (particle of light) couples with coherent oscillation of conduction electrons, a plasmon is created. Plasmon is a very short-lived quasi-particle. It lives for tens of femtoseconds at most, and decays back to a

photon or phonons (heat). Decay of the plasmon to a photon occurs in terms of light scattering. On the other hand, the decay of plasmon to phonon(s) is called absorption. Extinction is the sum of scattering and absorption:

$$\text{Extinction} = \text{Scattering} + \text{Absorbtion} \tag{2.6}$$

Within the context of the model mass-spring-damper system, extinction is the dissipated power that is balanced by the power nanoparticle extracts from the electromagnetic field. The power extracted from the field, is either dissipated to heat (absorption) or radiated back to the field (scattering).

From the point of power dissipation, plasmon extinction is caused by plasmon damping, which is characterized by Γ: the damping constant. Exploiting the Mathiessen's Rule, Γ can be split into scattering and absorption components as:

$$\Gamma = \Gamma_s + \Gamma_a \tag{2.7}$$

such that the scattered and absorbed power, P_s and , P_a, respectively, can be given by

$$P_s = P_{extinction}(\Gamma_s/\Gamma) \text{ and } P_a = P_{extinction}(\Gamma_a/\Gamma) \tag{2.8}$$

In this respect, plasmon decay or damping occurs either radiatively (scattering) or non-radiatively (absorption). As mentioned above, plasmon is a short-lived state with a time constant of ~10 fs. In simple terms, plasmon is a very "fragile" quasi particle whose decay or damping is very easy. Namely, any effect that disturbs the cohesive motion of "many" electrons contributing to the plasmon collapses the plasmon. In particular, radiative damping occurs when nanoparticle size is not sufficiently small compared to the wavelength. In this case, the phase of the electric field is not uniform throughout the nanoparticle, so is the phase of the electron motion. As a result, some electrons cannot

follow the others in phase and get “retarded”. Therefore, the plasmon collapses and releases its energy in terms of a photon. This is radiative plasmon damping, accounting for light scattering. Indeed, gold and silver nanoparticles larger than ~30 nm, experience significant radiative damping, which allow these particles be seen under optical microscope in dark field.

Non-radiative damping (absorption), on the other hand, occurs through a diversity of pathways. The most common mechanism for non-radiative damping is the scattering of electrons from defects and nanoparticle surface. Again, this scattering perturbs the cohesive electron motion. Though, the plasmon transfers its energy to an electron-hole pair instead of a photon. In turn, the energy of the electron-hole pair thermalizes to phonons (heat). Non-radiative damping can also take place through “chemical interface damping”, wherein the cohesive motion of the plasmon is perturbed by the trapping of some electrons in the adsorbate-induced quantum states. The adsorbate-induced states simply form by chemical bonding of guest atoms or molecules (from the environment) on the nanoparticle surface. The temporary “leakage” or “trapping” of the conduction electrons in these states dephases the plasmon and causes it to collapse. Again, the energy is thermalizes to phonons (heat).

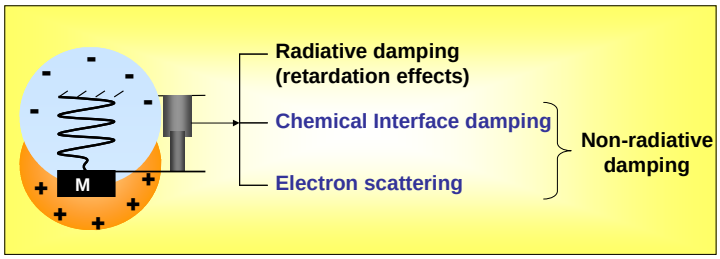

Figure 2.2: Schematic of “force-constant and damper model” analogy for the localized surface plasmon resonance (LSPR). Various damping mechanisms are listed.

The spring-mass-damper model for LSPR is depicted in Figure 2.2. In the operation of "hybrid plasmon damping sensor" of the present study, the sensing mechanism is not only due to chemical interface damping, but electron scattering. Electron scattering is simply caused by the perturbation of the electric potential at the surface of the nanoparticle by guest atoms or molecules (adsorbates).

2.2 Optical extinction

In the above discussion, plasmon extinction is introduced in terms of the power, which is captured by the nanoparticle from the electromagnetic field. On the other hand, in optical spectroscopy, "extinction" is defined as

$$E = -\log(T) \tag{2.9}$$

where T is the transmission, which is easy to measure using a spectrophotometer. When a light beam is blocked by a layer of nanoparticles, part of the light won't interact with the nanoparticles and be transmitted through (transmission). However, part of the light will be absorbed and scattered by the nanoparticles. In spectroscopy, the absorbed or scattered photons (light) are called the "extinct" photons (light) in the sense that they will not reach the detector in a simple transmission setup. In a medium where photons get extinct, the intensity of light decays exponentially in the propagation direction and the transmitted light will be: $I = I_o \exp(-\alpha d)$, where I, I_o and d are the transmitted and incident light intensities, and the distance traveled by light, respectively. The constant α is the "extinction coefficient", and is a measure of how intense the medium absorbs +

scatters the light. The exponential decay is simply the solution of differential equation that states; “rate of amount of light lost (absorbed + scattered) is proportional to its intensity” (Beer Lambert Law). Therefore, the extinction coefficient can simply be calculated from $\alpha d = -\log(I/I_o)$, where (I/I_o) is defined as the “transmission”, and αd is defined as the “extinction” as consistent with Equation 2.9.

Optical spectrometers are used to measure the transmission and extinction. In general, an optical spectrometer consists of a light source, from which the light is incident on the sample placed inside a cuvette holder. The intensity of the transmitted light is measured using a light detector. Figure 2.3 illustrates a schematic of the optical spectrometer used in the present study.

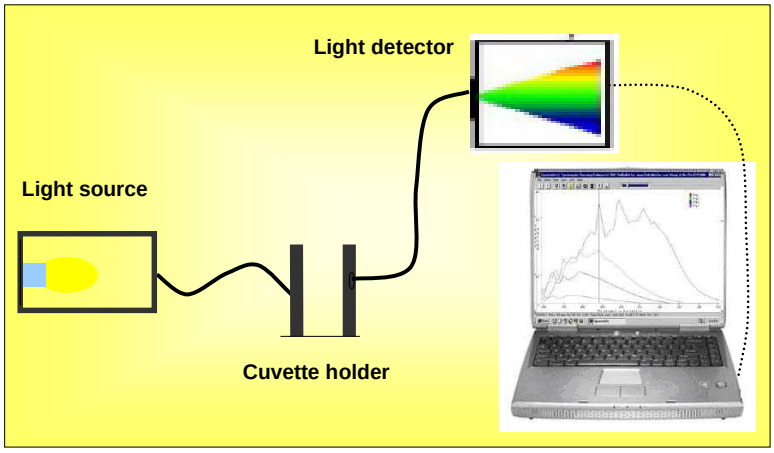

Figure 2.3: Measuring the optical extinction of a sample with an optical spectrometer.

In conclusion, extinction quantifies how strongly a medium absorbs and scatters the light. The significance of extinction is that, the measured plasmon extinction spectrum scales with $P_{extinction}$, which is given by Equation 2.5. Therefore, the damping constant, Γ, and total electron charge contributing to plasmon, Q, can be derived from extinction measurements. As will be clear in Chapter 3, once Γ and Q are extracted, the

total number of adsorbates on the nanoparticle surface can be quantified. In turn, concentration of the adsorbate in the ambient can be derived from the kinetics of adsorption.

2.3 Mie equation

In 1908, by fully solving for the Maxwell's Equations, Mie obtained an analytical solution for the extinction cross section of a solid sphere, σ_{ext}, in an electromagnetic field of angular frequency ω. In case the sphere's diameter is significantly smaller than the wavelength of light (e.g., 20 times smaller), σ_{ext} is given by

$$\sigma_{ext}(\omega) = 9\frac{\omega}{c}\varepsilon_m^{3/2}V\left(\frac{\varepsilon_2(\omega)}{[\varepsilon_1(\omega)+2\varepsilon_m]^2+\varepsilon_2(\omega)^2}\right) \qquad (2.10)$$

where $\varepsilon_1(\omega)+i\varepsilon_2(\omega)$ and ε_m are the dielectric functions for the sphere and the surrounding medium, respectively [1]. 'V is the sphere volume, and c is the velocity of light. σ_{ext} is defined such that, for a single nanoparticle, $P_{extinction} = I\sigma_{ext}$, where I is the irradiation or the light intensity (power per unit area).

Clearly, σ_{ext} has a resonance for $\varepsilon_1(\omega) = -2\varepsilon_m$, at $\omega = \omega_o$, that is known as the localized surface plasmon resonance (dipolar LSPR), while $\omega = \omega_o$ is called the plasmon frequency. Obviously, $\omega = \omega_o$ will shift with the variation in ε_m, since $\omega_o = \varepsilon_1^{-1}(-2\varepsilon_m)$. This forms the basis of detection for typical LSPR sensors.

Alternatively, σ_{ext} is subject to changes due to the changes in $\varepsilon_2(\omega)$ that is the basis for the novel detection technique developed in the present work.

The dielectric function for the metals can be approximated from free electron theory as

$$\varepsilon_1(\omega) = 1 - \frac{\omega_p^2}{\omega^2} \tag{2.11a}$$

$$\text{and } \varepsilon_2(\omega) = \frac{\omega_p^2}{\omega^3}\Gamma \tag{2.11b}$$

where ω_p is the bulk plasmon frequency and Γ is the phenomenological damping rate [1]. In vacuum and gases $\varepsilon_m \cong 1$, from which $\omega_o = \frac{\omega_p}{\sqrt{3}}$, $\varepsilon_1(\omega) = \frac{(\omega^2 - 3\omega_o^2)}{\omega^2}$, and $[\varepsilon_1(\omega) + 2] = \frac{3(\omega^2 - \omega_o^2)}{\omega^2}$. Using these relations and noting that $\left(\omega^2 - \omega_o^2\right)^2 \cong 4\omega_o^2(\omega - \omega_o)^2$ at the vicinity of resonance, the expression for σ_{ext} reduces to a Lorentzian:

$$\sigma_{ext} = \frac{3}{4}(V/c)\varepsilon_m^{3/2}\frac{\omega_o^2\Gamma}{(\omega - \omega_o)^2 + (\Gamma/2)^2} \tag{2.12}$$

As will be obvious in Chapter 3, Equation.2.12 as above is invaluable to the present work. It is noteworthy that, Equation 2.12 resembles Equation 2.5 which was derived from the equation of motion for the plasmon. Indeed, it is possible to derive Equation 2.12 from Equation 2.5 after several manipulations and using the relation $P_{extinction} = I\sigma_{ext}$.

2.4 Hybrid plasmon modes

An isolated metal nanoparticle, smaller than 30 nm, exhibits dipolar surface plasmon resonance, which occurs at the frequency $\omega_o = \frac{\omega_p}{\sqrt{3}}$ in free space, where ω_p is the bulk plasmon frequency as stated in the previous section. ω_p is given by Drude plasma frequency as $\omega_p = \sqrt{\left(\frac{4\pi e^2 N_e}{m_e}\right)}$ [1]. On the other hand, when two nanoparticles are close to each other, such that the interparticle separation is less than the particle diameter; the individual plasmon modes start to interfere and form two hybrid combinations: the symmetric mode is formed from in-phase dipole oscillations ($\omega_{h-s} < \omega_o$); and anti-symmetric mode from out-of-phase dipole oscillations ($\omega_{h-as} > \omega_o$)[11, 17], as illustrated in Figure 2.4. Because the net dipole moment of the anti-symmetric combination is zero for identical spheres, the anti-symmetric modes are not easily excited by light and observed (i.e., dark plasmons), in contrast to the symmetric hybrid plasmons (bright plasmons) [11, 14, 17, 22, 23]. Thus the optical extinction of hybrid plasmon mode is at lower frequency than regular plasmon mode. The frequency shift in the symmetric mode from the regular plasmon mode is obeys a universal relation of the form (plasmon ruler equation) [11, 17, 22]

$$\Delta\omega \propto -\left(\frac{D}{d}\right)^3 \tag{2.13}$$

$\Delta\omega = \omega_o - \omega_{h-s}$ denotes frequency shift between symmetric mode and regular plasmon mode, D is the metal nanoparticle diameter and d is the interparticle center to center distance. This scaling behavior can be explained by the dipolar coupling between the nanoparticles which is linear with particle polarizability (i.e., $\propto D^3$) as well as the dipolar electric field (i.e., $\propto d^3$) associated with each particle.

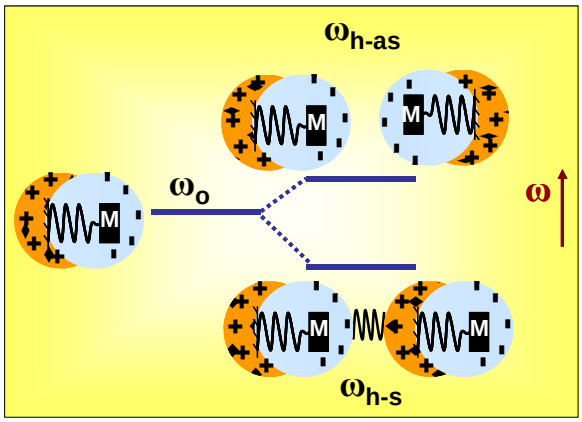

Figure 2.4: Schematics illustrating the hybridization of two dipolar plasmon modes ω_d into symmetric (lower energy) ω_{h-s} and anti-symmetric ω_{h-as} (higher energy) modes, when two identical nanoparticles come close to each other [11-22].

2.5 LSPR sensing mechanism - I

As derived in Section 2.3, LSPR peak occurs for the condition $\varepsilon_1(\omega) = -2\varepsilon_m$. Substitution in Equation. 2.11 yields

$$\omega_o = \frac{\omega_p}{\sqrt{1+2\varepsilon_m}} \tag{2.14}$$

Equation 2.15 suggests that the surface plasmon resonance peak (ω_o) shifts towards lower frequencies, when the refractive index of the medium surrounding nanoparticle increases [8, 9, 22, 24-26]. It is also evident from Equation 2.10 that the

optical extinction of the metal nanoparticles increases with increase in the refractive index of embedding medium ($\sigma_{ext} \propto \varepsilon^{3/2}$). This variation in the LSPR frequency induced by changes in refractive index of the near ambient of the nanoparticle has been exploited as a sensing mechanism by a number of research groups [3, 24-29]. In the framework of the oscillator model for LSPR, the frequency shift can be inferred from a decrease in the effective force constant, k. As illustrated in Figure 2.5, increase in polarizability (refractive index) of the medium induces attractive electric forces between the conduction electrons of the nanoparticle and polarized molecules. These new forces are in opposite direction with the original restoring force (between electrons and positive ion cores). As a result, the effective restoring force or force constant is reduced, shifting the resonance to a lower frequency.

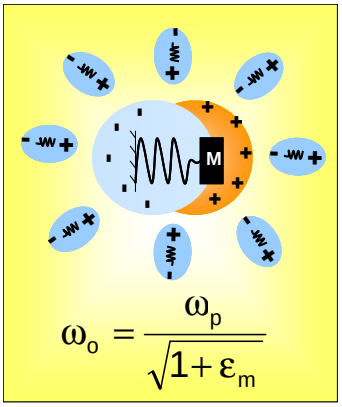

Figure 2.5: Schematic of LSPR sensing mechanism I. The increased polarizability (refractive index) surrounding the nanoparticle reduces the restoring force for the plasmon. As a result, the resonance frequency shifts towards lower values.

Amanda J. Haes and coworkers [24, 25, 30] used the frequency shift in the plasmon mode of the silver nanotriangles as LSPR sensor for detection of Alzheimer disease. The lower frequency shift in the optical extinction of the silver nanotriangles was used to determine the interaction of amyloid β-derived diffusible ligands (ADDL)

and anti-ADDLs which are involved in development of Alzheimer's disease. They confirmed that the plasmon frequency of the silver nanotriangles shifts towards red with increasing density and thickness of the adsorbate layers (ADDL and anti- ADDLs) [24, 25]. Okamoto et al, observed the optical frequency and intensity of the gold nanoparticles monolayer varies with refractive index of surrounding medium [31]. They concluded that the optical extinction of the monolayers of the gold nanoparticles shift towards red, when the refractive indices of the immersed liquids were increased. They also noticed that the intensity of the optical extinction of gold nanoparticles was increased with increase in the refractive index. Mock and coworkers demonstrated red shift in the spectrum of the individual silver nanoparticles with increase in the refractive index of oil surrounding the metal nanoparticles [32]. They also observed the spectrum of triangular shaped nanoparticle shifted more towards red than the dipole mode of spherical nanoparticles [32].

2.6 LSPR sensing mechanism -II

The other cause for variation in the frequency and the intensity of the LSPR is electron transfer between the adsorbate and nanoparticle. The direction of transfer depends on the Fermi level or electronegativity difference between the adsorbate and the metal nanoparticle [7, 10, 33-36].

From Drude plasmon frequency, $\omega_p = \sqrt{\left(\frac{4\pi e^2 N_e}{m_e}\right)}$, the bulk plasmon frequency increases with electron density, N_e. When electron transfer occurs towards the metal

nanoparticle, the surface plasmon resonance frequency shifts towards higher frequencies and vice versa [7, 10, 33-37]. In addition, the intensity of the optical extinction increases with increase in the number of conduction electrons.

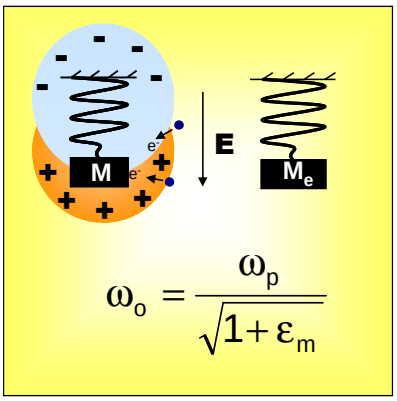

Figure 2.6: Schematic of the LSPR sensing mechanism II: electron transfer from the adsorbate to nanoparticle.

Henglein et al. [7, 10] during their study on bimetallic colloids observed surface plasmon frequency shifts towards higher frequency in the gold and silver nanoparticles, when the mercury was introduced in the nanoparticle colloidal solution. Morris et al. [12, 34-36] demonstrated that the optical extinction of dipolar plasmon mode of the silver nanoparticles blue shift more than gold nanoparticles. They also showed that the smaller particles exhibit more blue shift than larger particles. The authors suggested that the interactive nanoparticles are more sensitive to chemical adsorption than monodisperse nanoparticles.

As aforementioned, when the interparticle distance between two nanoparticles is less than the particle diameter, the individual plasmon modes start to interfere and form hybrid plasmon modes. In a recent study of Kalkan [38], it is shown that mercury exposure causes a high energy shift in dipolar plasmon mode whereas a lower energy shift in symmetric hybrid plasmon mode of the silver nanoparticles. The red shift in the

extinction of hybrid plasmon mode is due to increase in the electromagnetic coupling between particles. Once mercury donates electrons to metal nanoparticles, the intensity of the regular dipolar plasmon increases further enhancing the near fields surrounding the nanoparticles. Consequently, the plasmon interference between adjacent particles increases. As a result, the energy of the hybrid plasmon mode is further reduced.

Chapter 3

Methodology

3.1 LSPR sensing mechanism III

The present thesis work is centered around the development of a novel LSPR sensor that exploits a different sensing mechanism than the ones reviewed in the previous chapters. This novel LSPR sensor differentiates itself from others on the basis of two unique aspects. First, the sensor utilizes the hybrid plasmon mode (peak) as the sensing probe rather than the regular dipolar plasmon mode (peak). The present effort has succeeded in obtaining strong and well-resolved hybrid plasmon resonance exploiting its

innovative “nanometal-on-semiconductor” approach as well as its “electroless reduction on silicon” nanofabrication technique. As will be clear in Chapter 4, the hybrid plasmon resonance is more susceptible to damping by adsorbates.

Second, the LSPR sensor of the present effort makes use of a different sensing mechanism. Unlike previous LSPR sensing demonstrations, which monitor frequency shifts due to either refractive index or electron density changes (referred as LSPR sensing mechanisms I and II in Chapter 2), the present sensor probes two measurables: 1) the hybrid plasmon damping, which is full width at half maximum (FWHM) of the optical extinction peak of the hybrid mode; 2) the intensity of the extinction peak for the hybrid mode. Once these two parameters are recorded, a theoretical calculation, also developed in the present thesis, is performed to precisely quantify the number of electrons gained or lost by the hybrid plasmon mode.

For example, when one mercury atom adsorbs on silver, it donates exactly one electron to the plasmon mode, while a H_2S molecule steals exactly two electrons. Therefore, by “counting” the electrons contributing to the hybrid plasmon, one can precisely quantify the number of adsorbate atoms or molecules on the silver surface. On the other hand, monitoring or deriving the changes in resonance frequency, refractive index, electron density, or just damping, does not precisely quantify the number of adsorbates. This is because the relationships between these parameters and the number of adsorbates are nonlinear and often complex.

3.2 Calculation of the number of adsorbates

Next, the Author would like to disclose the calculation he developed for the calculation of number of adsorbates. This calculation originates from Equation. 2.13, which is the Lorentzian derived for σ_{ext}:

$$\sigma_{ext} = \frac{3}{4}(V/c)\varepsilon_m^{3/2} \frac{\omega_o^2 \Gamma}{(\omega - \omega_o)^2 + (\Gamma/2)^2} \tag{2.13}$$

At resonance ($\omega = \omega_o$), $\sigma_{ext} = \sigma_{ext,peak} = \left(3V\varepsilon_m{}^{3/2}/c\right)\frac{\omega_o^2}{\Gamma}$. Remembering $\omega_o = \frac{\omega_p}{\sqrt{3}}$ and using the fact that plasmon frequency scales with the square of the electron density, $\omega_p = \sqrt{\left(\frac{4\pi e^2 N_e}{m_e}\right)}$ [1],

$$\sigma_{ext,peak} = \left(\frac{4\pi e^2 V \varepsilon_m{}^{3/2}}{c m_e}\right)\frac{N_e}{\Gamma} \tag{3.1}$$

When a molecule adsorbs on the nanoparticle, it changes both N_e and Γ from N_{eo} to $N_{eo} + \Delta N_e$ and from Γ_o to $\Gamma_o + \Delta\Gamma$. Hence,

$$\sigma_{ext,peak} \propto \frac{N_{eo} + \Delta N_e}{\Gamma_o + \Delta\Gamma} \tag{3.2}$$

As discussed in Chapter 2, $\Delta\Gamma$ results from local distortion of the surface electric potential by the adsorbate or chemical interface damping [1, 7, 10, 39-41].

The impact of adsorption on N_e depends on the type of bond established. 1) Positive ΔN_e. This occurs when the adsorbate contributes to the plasmon mode with

free electron(s). Typically, metallic bonds account for this. As an example, mercury has high affinity for silver, and establishes a metallic bond contributing an electron to the conduction electron gas. Since this electron becomes completely delocalized in the silver nanoparticle, ΔN_e is the number of mercury atoms adsorbed; i.e., $\Delta N_e = N_{Hg}$ 2) Negative ΔN_e. This occurs when covalent bond(s) are established. Since, silver shares electron(s) with the adsorbate and these electrons are strongly localized in the covalent bond(s), the number of free electrons associated with the plasmon is reduced. A good example of this is the adsorption of H_2S on silver. This involves the chemical reaction:

$$2Ag + H_2S \rightarrow Ag_2S + H_2$$

For each sulfur chemisorbed on the silver surface, 2 free electrons from silver metal are stolen to 2 Ag–S bonds. In other words: $\Delta N_e = -N_{Ag-S} = -2N_S$. 3) $\Delta N_e \cong 0$ (Physisorption). Both Case (1) and Case (2) are associated with chemisorption, where electron sharing takes place between the nanoparticle and the adsorbate. One may ask: "how does N_e change upon physisorption? Physisorption is due to Vander Waals or dipole – induced dipole bonds, which do not involve electron sharing or transfer. Therefore, physisorption can at most change the local polarizability or refractive index around the particle, leading to a shift in ω_o. However, a change in N_e is not expected. Further, physisorption can perturb the electric potential at the nanoparticle surface dephasing the plasmon. Hence, physisorption is detectable from increase of damping: $\Delta\Gamma$.

As stated in Chapter 2, in the absence of heterogenous broadening of the plasmon resonance, extinction equals σ_{ext} multiplied with a constant. Therefore, it follows from Equation. 3.2 that

$$H = C\frac{N_{eo} + \Delta N_e}{\Gamma} \tag{3.3}$$

where H is the extinction peak and C is the scaling factor. Therefore,

$$C\Delta N_e = H\Gamma - CN_{eo}$$

If $H_o = C\frac{N_{eo}}{\Gamma_o}$ is the intrinsic (in the absence of adsorbates) extinction peak intensity, then $CN_{eo} = H_o\Gamma_o$. Accordingly, $\Delta N_e = (H\Gamma - H_o\Gamma_o)/C$. Eliminating C,

$$\Delta N_e = N_{eo}\left(\frac{H\Gamma}{H_o\Gamma_o} - 1\right) \tag{3.4}$$

As we discussed above, for the chemisorption of mercury on silver, we have $\Delta N_e = N_{Hg}$. Therefore,

$$\Delta N_{Hg} = N_{eo}\left(\frac{H\Gamma}{H_o\Gamma_o} - 1\right) \tag{3.5}$$

where N_{Hg} stands for the number of mercury atoms chemisorbed, while N_{eo} equals the total number of electrons contributing to the plasmon regardless of plasmon being a regular dipolar plasmon or hybrid plasmon. In the case of hybrid plasmon, it is difficult to guess how many interacting nanoparticles contribute to the plasmon.

In summary, the scheme developed here calculates the number of adsorbates simply from the product of $H\Gamma$, which can easily be extracted from the plasmon

extinction spectrum: (peak intensity)×(full width at half maximum). Because the above expression derives directly from theory, no artificial fitting parameters are needed. Although, the derivation above is essentially performed for a single isolated nanoparticle, the hybrid plasmon resonance is also of Lorentzian character and characterized with certain values of ω_o, Γ, H, and N_e. Therefore, Equation. 3.5 applies to hybrid surface plasmon resonance, too electron transfer. The variation in the damping due to adsorbates can be determined from optical extinction if the intrinsic plasmon damping is sufficiently reduced. When the intrinsic damping is reduced significantly, damping due to molecular adsorption becomes prominent and causes a subsequent decrease in hybrid plasmon extinction. Hence, the present study attempts to control the damping of the optical extinction associated with hybrid plasmon mode by process of annealing.

3.2 Deposition of reducer film

Monolayers of silver nanoparticles were synthesized on 100 nm thick hydrogenated amorphous silicon films coated on glass. Silicon serves as the reducer for the reduction of Ag^+ ions to Ag nanoparticles. The silicon film deposition was performed by United Solar Ovonic (Auburn Hills, Michigan) using an Applied Kamatsu plasma-enhanced chemical vapor deposition system (model AKT 1500 A). H_2 diluted silane (H_2:SiH_4) (4:1) was employed as the precursor. The deposition was carried out at a substrate temperature of 150 ºC, at a deposition rate of 10 nm/s on Corning code 7059 glass substrates [42].

3.3 Synthesis of nanoparticles

The silver nanoparticles were synthesized by immersion of hydrogenated amorphous silicon films in silver nitrate solution. The silicon film serves as a reducer as well as it immobilizes the nanoparticles. As mentioned in Chapter 1, this electroless reduction process provides "clean", surfactant-free nanoparticles. Once charge transfer occurs between silver and silicon due to Fermi level difference, the opposite charging between the silver and silicon anchors the nanoparticles to the silicon film without the need for a binding agent. At the same time, the repulsion between the nanoparticles (due to the same charge polarity) prevents the aggregation or impingement of the nanoparticles despite the fact that the interparticle spacing can get as low as few nm. As a result, the synthesized silver monolayers possess strong and well-resolved hybrid plasmon extinction. All of these advantageous attributes follow from the combination of two novel nanofabrication approaches employed in the present thesis: "electroless reduction" and "nanometal-on-semiconductor".

Silicon films deposited on glass substrates were cut to 5mm×10mm samples, so that they could be accommodated inside standard 4 mL optical cells once nanoparticle synthesis is completed. Then the substrate was cleaned in iso-propanol under ultrasonication for removal of organic impurities. Subsequently, the film was rinsed with de-ionized water and treated with 5% HF for removal of the native oxide layer. For the synthesis of silver nanoparticles, the silicon films were immersed in 0.002 M $AgNO_3$ solution containing 0.1% HF [18]. The reason for including HF is to etch silicon oxide formed during the redox reaction. The $AgNO_3$ purchased from Sigma Aldrich, was

dissolved in 18.2 MΩ de-ionized water. Then, HF obtained from J.T. Baker was added in appropriate proportion. The reaction was stopped by immersing the films in de-ionized water. Finally, the samples were dried using a nitrogen blow gun.

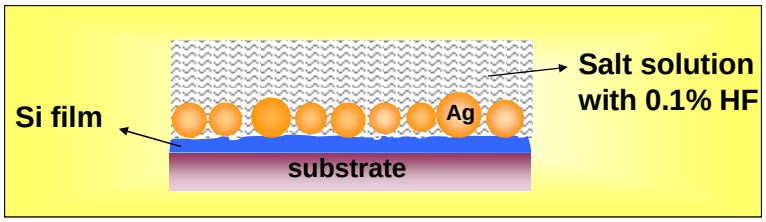

Figure 3.1: Synthesis of silver nanoparticles on silicon film.

3.4 Annealing of the nanoparticles

Subsequent to nanoparticle synthesis, optical extinction spectrum of the virgin nanoparticles was recorded. A StellarNet EPP 2000Cs UV-Vis spectrophotometer with a CCD detector was employed for the optical extinction measurements. The sample was placed inside a glass optical cell and the extinction spectrum was determined using optical spectrometer. Using a small stainless steel spring, the sample was fixed to the optical cell wall. Optical extinction of the silver nanoparticles was obtained by subtracting the extinction (-log (transmission)) of silicon substrate without nanoparticles from the extinction of silicon substrate with nanoparticles. The subtraction was carried out by the Spectrawiz graphical user interface software of optical spectrometer. Before capturing extinction, the integration time was adjusted to maximize detector output and signal to noise ratio without saturation of the detector. It was set to 150 ms, and for further increasing signal to noise ratio an accumulation of 10 spectral measurements was recorded. Once the extinction spectrum was obtained, the sample was annealed on the

hot plate at 300° C for 1 min as seen in Figure 3.2. Subsequently, the optical extinction was measured again.

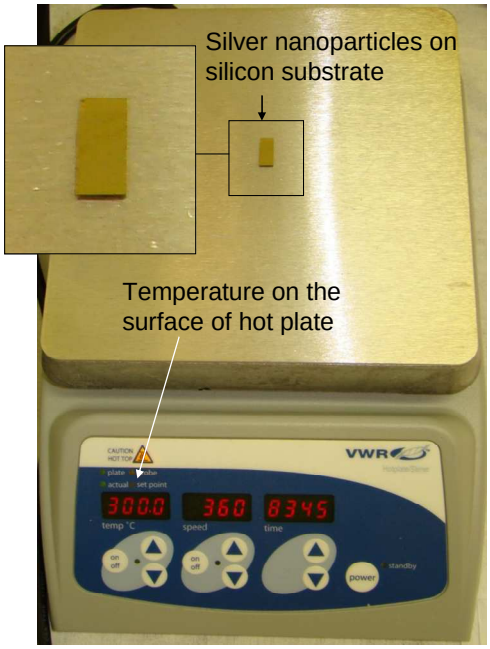

Figure 3.2: Annealing of the silver nanoparticles synthesized on the silicon film using a hot plate. The inset shows the closer view of silicon film (with silver nanoparticles synthesized on it).

3.5 Purging of samples using nitrogen/argon

The annealed sample was then placed in the optical cell and spring-loaded. In order to fill the optical cell with nitrogen or argon, the setup shown in Figure 3.3 was used. Two syringe needles were pierced into the septum of the optical cell with one of them connected to nitrogen/argon gas cylinder and the other opened to air nitrogen/argon gas pressure was regulated to a pressure of 1 psi allowing the flow of nitrogen/argon into the optical cell. Thus, air inside the cell was purged out through the other syringe needle. After purging the air for 10 min or more, the syringe needle that opened to air was

removed first. Then, the syringe needle connecting to the nitrogen cylinder was removed from the septum.

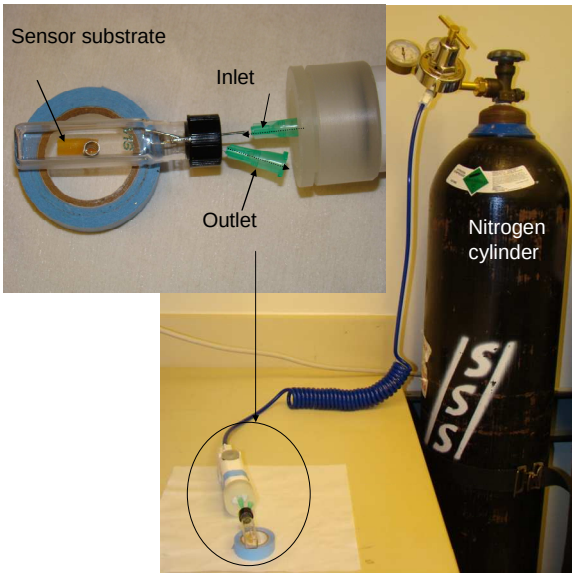

Figure 3.3: Picture of the experimental setup for purging of the optical cell, which encloses the sensor. The inset shows the arrangement of inlet and outlet syringe needles.

3.6 Exposing the nanoparticles to mercury vapor

Once purging is complete, the extinction of silver nanoparticles is recorded in pure nitrogen/argon medium. Subsequently, 1 g of mercury (from Alfa Aesar) was injected into the optical cell using a syringe and extinction was recorded periodically while the optical cell is kept in the cuvette holder of optical spectrometer. The mercury vaporizes inside optical cell at room temperature and reaches a saturation level of 15 ppm ($15\,ng/mL$) [35, 43]. The saturation level is estimated to reach in less than 2minutes in 4mL optical cell (approximating surface area mercury droplet to be $0.5cm^2$ evaporates at a rate of $5\mu g/cm^2/h$ at 20°C) [44]. The optical extinction measurements were taken from the instant mercury is injected in the cell.

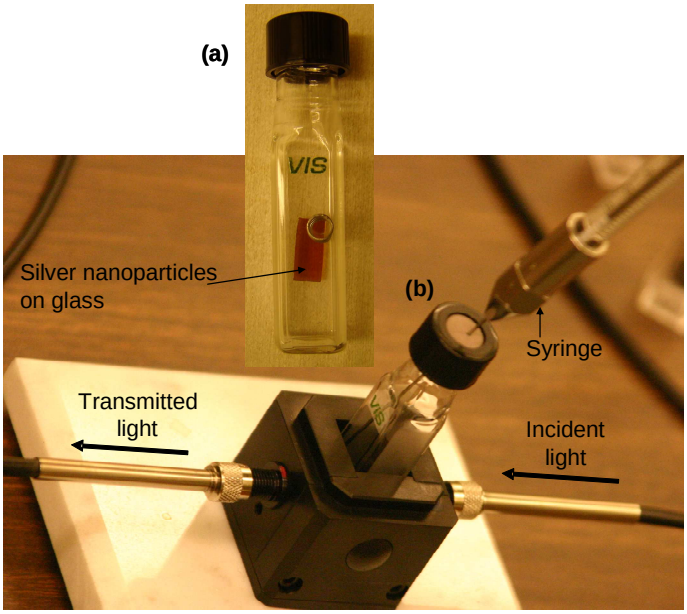

Figure 3.4: Picture shows: (a) the optical cell with sensor substrate immobilized inside by a wire spring; (b) injection of mercury into the optical cell, which is placed in the cuvette holder while the optical extinction measurement is in progress.

Chapter 4

Results and Discussion

4.1 Nanoparticle synthesis

The silicon film (deposited on glass as described in Section 3.2) was immersed in 0.002 M $AgNO_3$ for 5s, 10s and 20s for synthesis of silver nanoparticles as elaborated in Section 3.3. These nanoparticles were imaged with a Digital Instruments Nanoscope IIIa Multimode atomic force microscope operating in tapping mode. Figure 4.1 shows the AFM images of the silver nanoparticles obtained for different immersion times.

From the AFM image, the size and distribution of silver nanoparticles for different immersion times are elucidated. Evidently, the size of the silver nanoparticles increased with increasing immersion time. The average sizes of the silver nanoparticles are measured to be 21, 28 and 33 nm for 5, 10 and 20 s of immersion times respectively. Once corrected for tip effects, the nanoparticle sizes are estimated to be 80% of the given values [38].

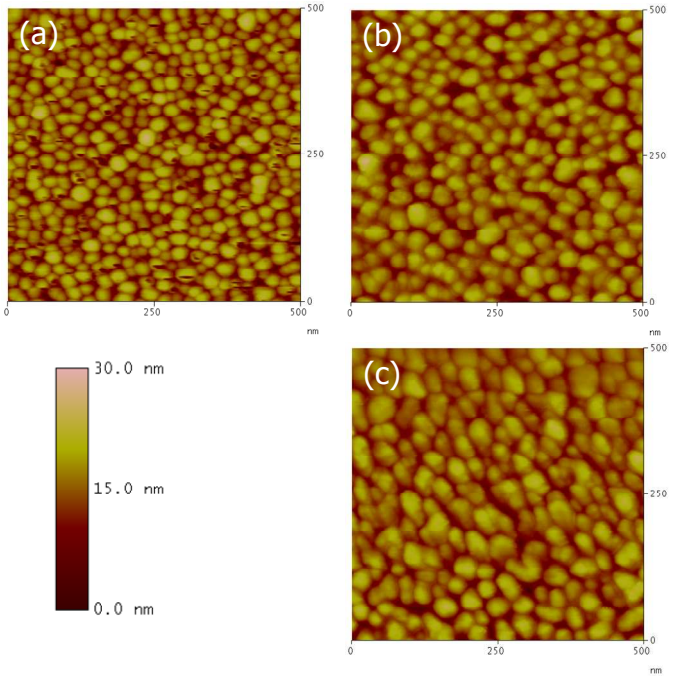

Figure 4.1: AFM images of silver nanoparticles synthesized by electroless reduction on silicon films for different immersion times in salt solution: (a) 5s; (b) 10s; and, (c) 20s [38].

The AFM images also show that silver nanoparticles are very closely distributed which would lead to the formation of hybrid plasmon modes. The silicon film in the present synthesis mechanism, not only serves as a reducer, but also immobilizes the silver nanoparticles by opposite charging of silver (+) and silicon (–) due to Fermi level difference. The Coulombic repulsion between the nanoparticles prevents coalescence, although the interparticle separation gets very small compared to particle diameter during

synthesis. As a result, strong electromagnetic coupling develops between the nanoparticles, leading to intense hybrid plasmon modes, as observed from optical extinction [11].

4.2 Minimization of damping

The annealing has been found to lead to a dramatic reduction of the intrinsic hybrid plasmon damping in silver nanoparticles. Figure 4.2 shows the optical extinction of the silver nanoparticles before and after annealing processes. The peaks of optical extinction located at 590 nm are assigned to hybrid plasmon resonance. The damping factor or full width at half maximum of the hybrid peak is found to narrow from 0.72 to 0.48 eV upon annealing.

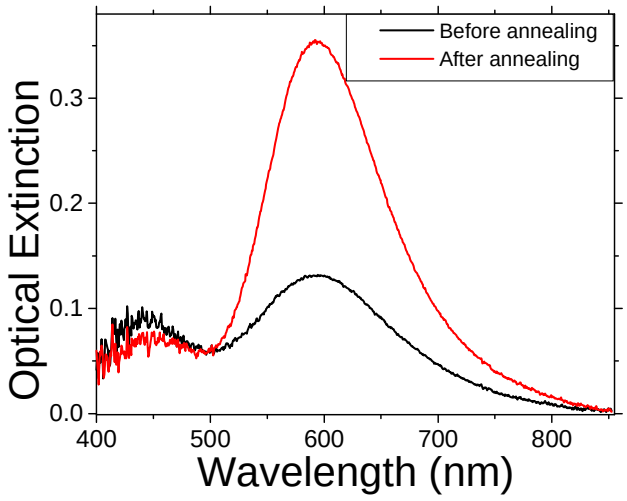

Figure 4.2: Optical extinction spectra before and after the annealing of the silver nanoparticles.

Figure 4.3 depicts the restructuring of silver nanoparticles during the annealing step. Evidently, sintering of the nanoparticles has occurred leading to average particle size increasing from 28 to 52 nm. The red shift of the regular plasmon band (i.e., shorter wavelength band) with annealing is consistent with the particle growth. Upon annealing, the optical extinction associated with the hybrid plasmon mode is seen to increase by a factor of 1.85 as observed from Figure 4.2. This observation is also ascribed to decrease in hybrid plasmon damping in consistent with Equation 3.3.

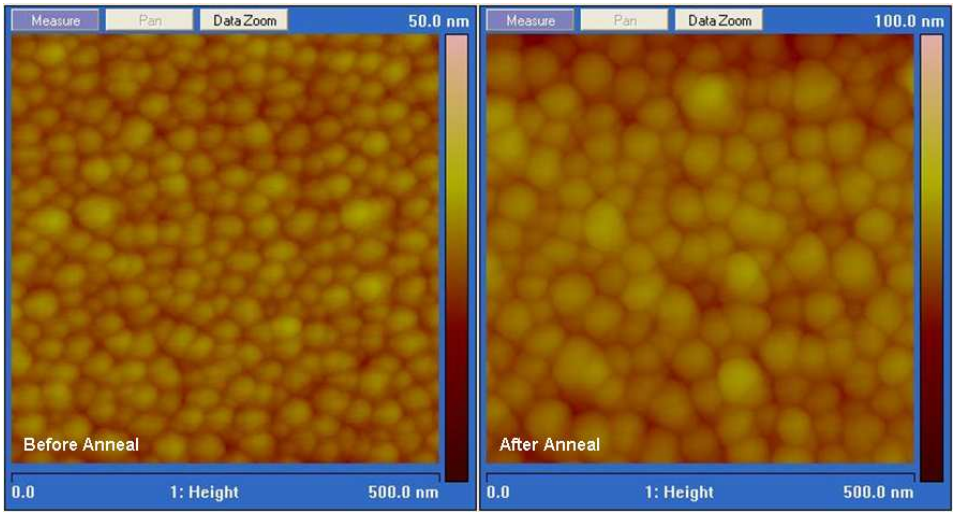

Figure 4.3: AFM images of silver nanoparticles: (a) before annealing; and, (b) after annealing. Nanoparticles were synthesized by a 10s immersion step [46].

The reduction of intrinsic damping can result from a decrease in dephasing (radiative damping), or decrease in electron scattering (non-radiative damping), or both. At first, the particle increase seen in Figure 4.3 is contrary to the observed decrease in damping. This is because, the retardation effects (leading to radiative damping) in single metal nanoparticles increase with increase in size. However, it is possible that, the restructuring in interacting nanoparticle systems (i.e., increase in) may account for decrease in the overall radiative damping of hybrid plasmon mode despite an increase in

average particle size. This decrease in radiative damping can take place due to the establishment of optimum particle size and center to center distance as observed by others [45]. Indeed, this argument is proven by light scattering measurements in the next section.

Further, decrease in damping can also be due to decreased electron scattering by rectification of structural defects like dislocations and grain boundaries at higher thermal energy. Figure 4.4 shows TEM micrographs of representative single silver nanoparticles before and after anneal. Evidently, structural defects, such as grain boundaries and twins are present in both cases. Hence, it is not clear whether the role of low temperature anneal is reduction of structural defects.

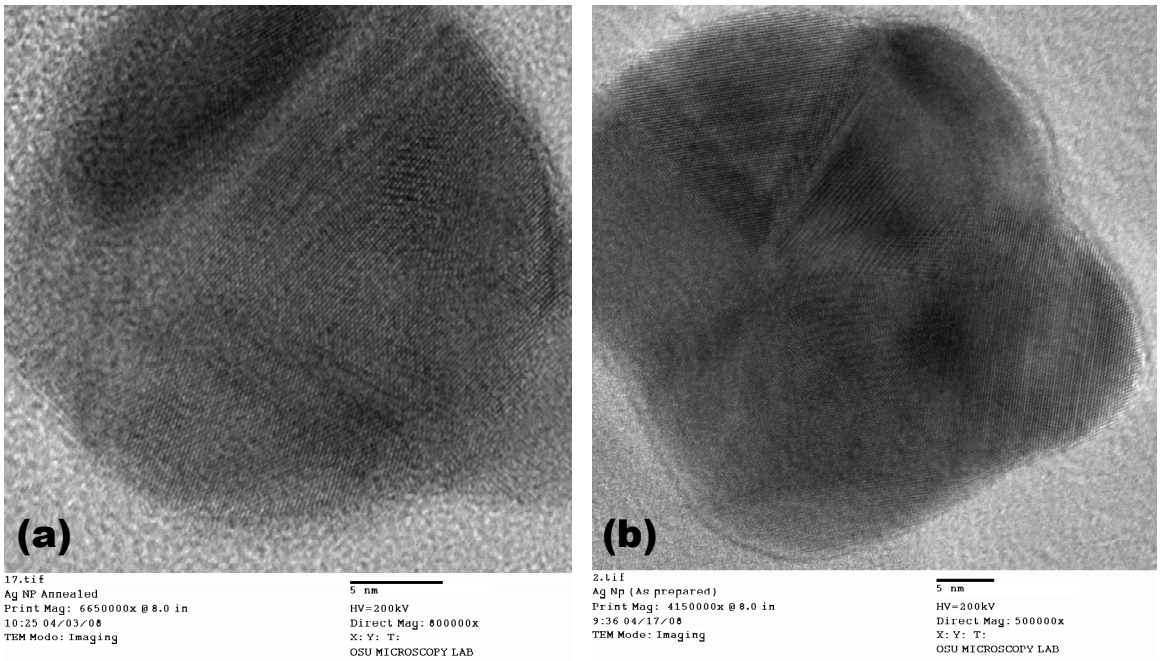

Figure 4.4: High resolution TEM micrographs of representative silver nanoparticles (a) before and (b) after anneal.

Figure 4.5 shows the optical extinction of the silver nanoparticles annealed for different time intervals at 300 ºC. After several replications, it is concluded that, annealing above 1 min is not beneficial. Rather, longer annealing times lead to increase

in hybrid plasmon damping, likely due to oxidation of the silver surface (non- radiative damping).

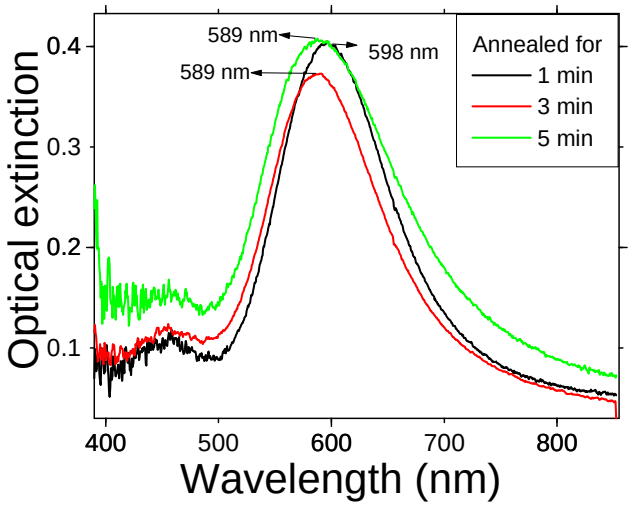

Figure 4.5: Optical extinction spectra of the silver nanoparticles annealed on the hot plate for different time intervals.

4.3 Estimation of decrease in radiative damping due to annealing

The decrease in radiative damping due to annealing was estimated by conducting light scattering measurements. Scattered light was collected from both the annealed and unannealed sample using a Renishaw RM 1000 Raman spectrometer fitted with Leica DMLM microscope. Spectral measurements were recorded under tungsten-halogen illumination with exposure time of 0.02 s, an accumulation of 100 scans. A 150 l/mm grating and high confocality mode was employed during the measurement. After subtraction of background, the ratio of scattered powers after annealing and before annealing $P_{s,aa}/P_{s,ba}$ was computed. Then, the ratio of damping constants before and after annealing was obtained. Combining Equation. 2.8 and Equation. 3.1, one

has $P_s \propto \Gamma_s / \Gamma^2$. Therefore, the ratio of radiative damping for annealed to unannealed silver nanoparticles are obtained as

$$\frac{\Gamma_{s,aa}}{\Gamma_{s,ba}} = \left(\frac{P_{s,aa}}{P_{s,ba}}\right) \times \left(\frac{\Gamma_{aa}}{\Gamma_{ba}}\right)^2 \tag{4.1}$$

Where $\Gamma_{s,aa}$ and $\Gamma_{s,ba}$ are radiative damping contants after and before anneal, respectively. Figure 4.6 displays the plot for $\frac{\Gamma_{s,aa}}{\Gamma_{s,ba}}$ once measured data are substituted in Equation 4.1.

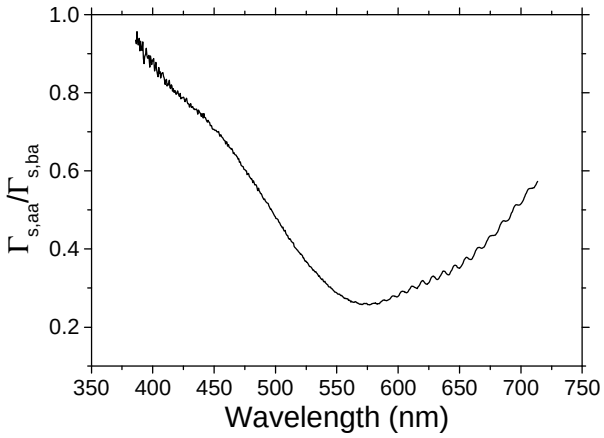

Figure 4.6: Plot of $\Gamma_{s,aa} / \Gamma_{s,ba}$ computed from equation 4.1

Figure 4.6 suggests a decrease in the radiative damping for the annealed silver nanoparticles. The decrease in radiative damping is thought to be due to restructuring of monolayer of silver nanoparticles as discussed above. In particular, the reduction is maximum at around the hybrid resonance wavelength of 580 nm. The minimization of hybrid plasmon damping is a substantial benefit from sensitivity point of view. Once the

intrinsic damping is minimized, adsorbate-induced damping can be resolved and detected at lower concentrations.

4.4 Sensor response to mercury vapor in air

The fabricated hybrid plasmon damping sensors were tested for mercury vapor as detailed in Section 3.4. Figure 4.7 shows the optical extinction spectra of a silver nanoparticle monolayer measured for every 5minutes (0 to 120minutes) after the introduction of 1 g mercury bubble in the optical cell. It is concluded from the figure, that the extinction of the hybrid plasmon mode decreases (an 8% decrease is recorded in 30s after mercury exposure) and regular dipolar plasmon mode blue shifts with time. The vaporized mercury atoms adsorb on the silver nanoparticles and adsorption of mercury leads to increase in damping. The increase in damping in turn decreases the extinction of hybrid plasmon mode. Silver being more electronegative than mercury, electrons are donated by the mercury to the silver nanoparticle; increasing total number of conduction electrons N_e in silver. This change in the number of conduction electrons also increases bulk frequency ω_p accounting for the blue shift of dipolar plasmon mode [7, 10, 33-37].

From Equation 3.1 or 3.3, the relationship between intensity of the plasmon extinction peak and the damping and the number of adsorbates is elucidated. Adsorption of mercury atoms on the sintered silver nanoparticles increases additional damping $\Delta\Gamma$.

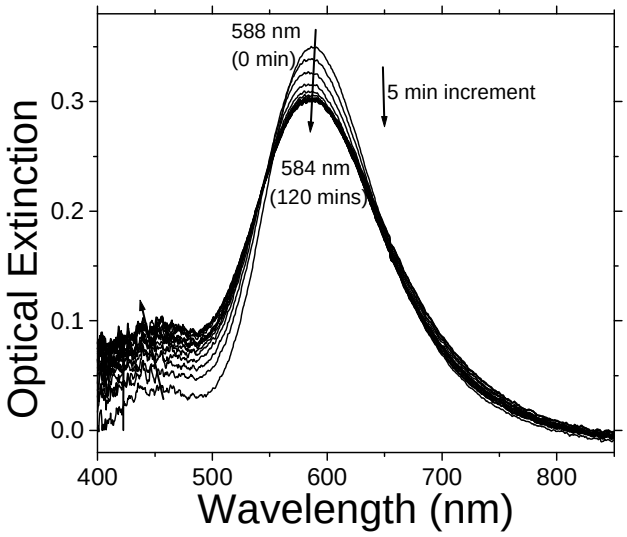

Figure 4.7: Optical extinction spectra (for every 5 minutes from 0 to 120 minutes) of the silver nanoparticles in air medium being exposed to mercury [46].

4.5 Sensor response to mercury vapor in nitrogen

Figure 4.8 shows the optical extinction spectra (measured for every 5 minutes from 0 to 120 minutes) of the mercury adsorbed silver nanoparticles in nitrogen medium. By comparing Figure 4.7 and 4.8, we can infer that the hybrid plasmon mode extinction in case of silver nanoparticles in nitrogen medium decreases faster with time. This is possibly due to the competition of mercury with oxygen and water in air ambient for adsorption on silver.

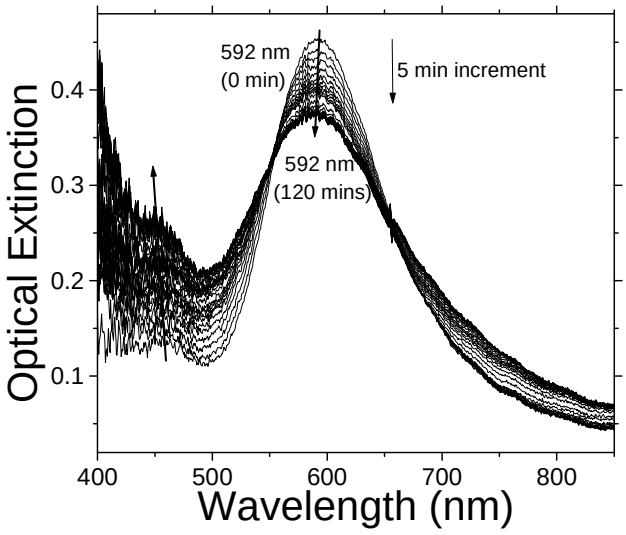

Figure 4.8: Optical extinction spectra (for every 5 minutes from 0 to 120 minutes) of the silver nanoparticles in nitrogen medium being exposed to mercury.

4.6 Measurement of extinction, damping constant and extraction of ΔN

The measured optical extinction of the silver nanoparticles in air, nitrogen and argon medium were fitted to Lorentzians using a computational algorithm. H, extinction peak height (corrected height after background subtraction) and Γ, damping factor were obtained by least squares curve fitting technique. Subsequently, Equation 3.5 was exploited to compute the number of mercury adsorbates (ΔN):

$$\Delta N = N_o\left(\frac{H\Gamma}{H_o\Gamma_o} - 1\right) \tag{3.5}$$

H, Γ, and normalized number of adsorbates $\frac{\Delta N}{N_o}$ were plotted as a function of time as shown in Figures 4.9, 4.10 and 4.12.

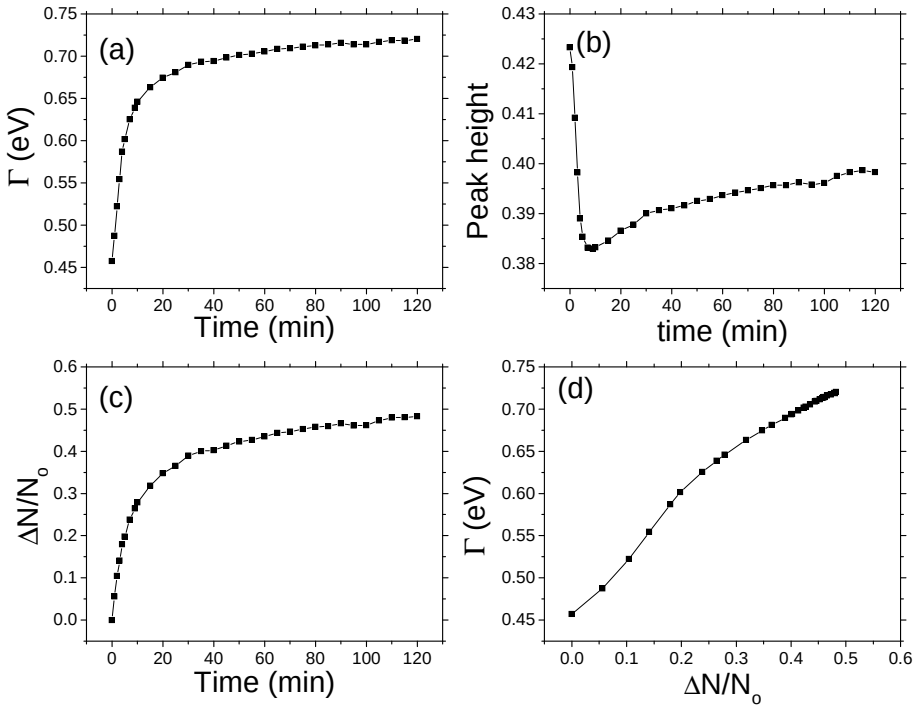

Figure 4.9: Kinetics of (a) damping, (b) peak height of hybrid plasmon extinction of the silver nanoparticles exposed to mercury in air. (c) The number of mercury adsorbates as a function of time. (d) Variation of damping with number of adsorbates.

It is evident from the Figure 4.9 (a) and 4.9 (c) that the damping and number of adsorbates increases initially and reaches a saturation value. These two parameters follow Langmuir adsorption isotherm pattern.

$$\Delta N = N\frac{K_{ad}}{K_{ad}+K_{de}}\left(1-e^{-(K_{ad}+K_{de})t}\right) \tag{4.2}$$

whereas K_{ad} and K_{de} are adsorption and desorption rate coefficients. Figure 4.9 (b) depicts the trend of the peak height due to mercury adsorption; it decreases initially (for first 10 minutes), after reaching minimum, it increases steadily with time and later, it reaches saturation, after filling all the adsorption sites. The intensity of the plasmon extinction peak can vary due to (from Equation 3.2): 1) electron transfer between the

adsorbate and the nanoparticle (numerator); and 2) increased damping due to the increased scattering of the electrons by the adsorbate (denominator). From Figure 4.9 (b) it is found that the role of the increasing damping factor increases and becomes dominant with the adsorption of mercury atoms on the silver nanoparticles. Further, $N_o + \Delta N$ also increases due to transfer of electrons from mercury atoms to silver nanoparticles, increasing the conduction electrons in silver nanoparticles. Each adsorbed mercury atom contributes an electron to the silver nanoparticle, so ΔN is linear with the number of adsorbed mercury atoms. In addition, if it is assumed the damping rate is linear with the number of adsorbates; i.e. $\Delta\Gamma = c\Delta N$ then Equation 3.2 becomes

$$\sigma_{ext,peak} = k\frac{N_o + \Delta N}{\Gamma_o + c\Delta N} \tag{4.3}$$

From the Equation 4.3 it can be deduced that $\sigma_{ext,peak}$ should only either decrease or increase with ΔN which is contrary with our results. Hence the assumption that damping rate varies linearly with number of adsorbates is invalid and the damping varies sub-linear with number of adsorbates [46]. Aforementioned relation between damping and number of adsorbates is also fortified from Figure 4.9 (d).

Figure 4.10 displays the kinetics of the damping, peak height and number of adsorbates when the sensor is exposed to mercury vapor in argon gas. H and Γ are seen to follow the similar trend as when the sensor is exposed to mercury in air. However, $\Delta N/N_o$ shows a significant deviation from a regular Langmuir isotherm as described by Equation 4.2.

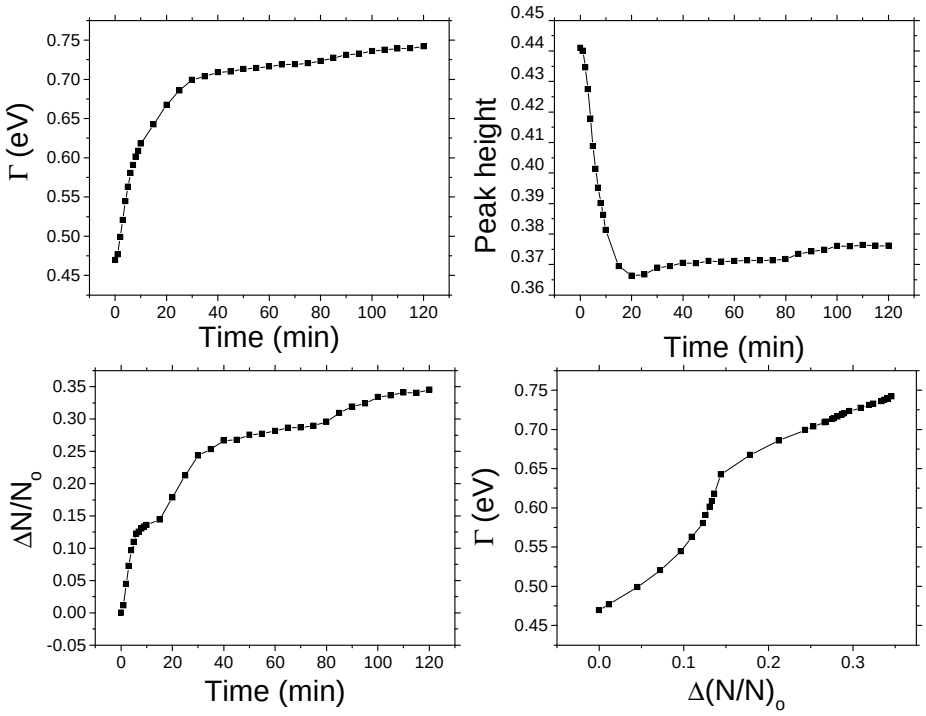

Figure 4.10: Kinetics of (a) damping, (b) peak height of hybrid plasmon extinction of the silver nanoparticles exposed to mercury in argon. (c) The number of mercury adsorbates as a function of time. (d) Variation of damping with number of adsorbates.

Equation 4.2 governs the net adsorption kinetics of gas atoms/molecules on a solid surface which is known as Langmuir adsorption isotherm. The variation of number of adsorbates with time (Figure 4.10 (c)) can be resolved into superposition of multiple Langmuir isotherms. In Figure 4.11, the variation of number of adsorbates with time is fitted to the superposed multiple Langmuir isotherms. Each isotherm denotes the crystal facets of silver nanoparticles whose rate of adsorption/desorption are different from each other. The adsorption of an atom/ molecule on solid surface also depends upon surface energy of crystal facets. It also suggests that the individual Langmuir isotherms origin at different times, this may be because of filling higher energy facets initially and lesser energy facets later.

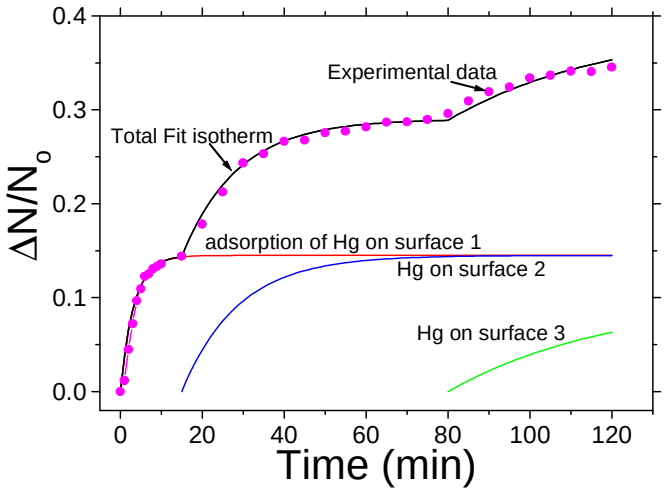

Figure 4.11: Number of mercury adsorbates with time (in argon gas). The kinetics is fitted to Langmuir isotherm

Figure 4.12 shows the variations of the parameters damping, peak height and number of adsorbates in nitrogen medium. The sensor in the nitrogen gas also shows similar characteristics of sensor in the argon gas medium. In Figure 4.12 (c) variation of number of adsorbates with time is a reminiscent of multiple Langmuir isotherms. This combination of multiple Langmuir isotherms is shown in Figure 4.13.

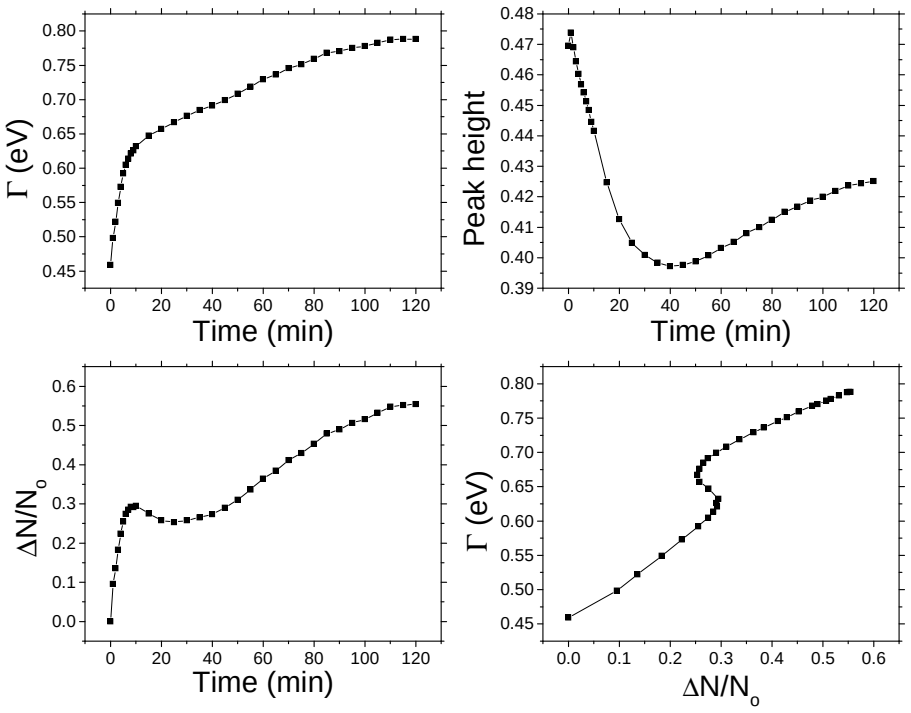

Figure 4.12: Kinetics of (a) damping, (b) peak height of hybrid plasmon extinction of the silver nanoparticles exposed to mercury in nitrogen. (c) The number of mercury adsorbates as a function of time. (d) Variation of damping with number of adsorbates.

The time variation of number of adsorbates is also reminiscent of multiple Langmuir isotherms superposed for sensor in nitrogen gas. This behavior may result from of dissimilar adsorption sites/rates (e.g., surfaces with different crystal orientations). As fitted in Figure 4.11, the variation of number of adsorbates with time is fitted to the superposed multiple Langmuir isotherms. From Figure 4.13, one of the isotherms in the fitted curve shows the adsorption of nitrogen in the medium. Even though nitrogen molecule has triple bond between them, according to recent Noble laureate Gerhard Ertl, nitrogen during formation of ammonia molecule breaks into individual atoms at the crystal surface of catalyst [47-49]. The negative trend in the number of adsorbates is

because N is covalently bonding with silver and arresting electrons, which are otherwise free and contribute to the plasmon.

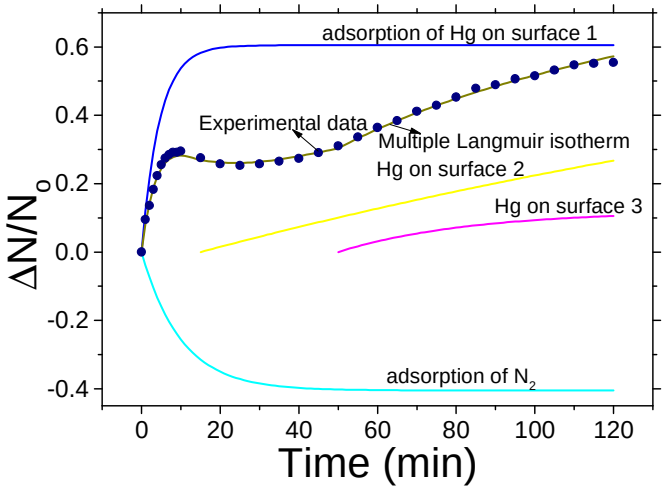

Figure 4.13: Number of mercury adsorbates with time (in nitrogen gas). The kinetics is fitted to Langmuir isotherm.

Further, Figures 4.14 (a), (b) and (c), shows the comparison between amount of damping energy and number of adsorbates as function of time for silver nanoparticles in air, nitrogen and argon media.

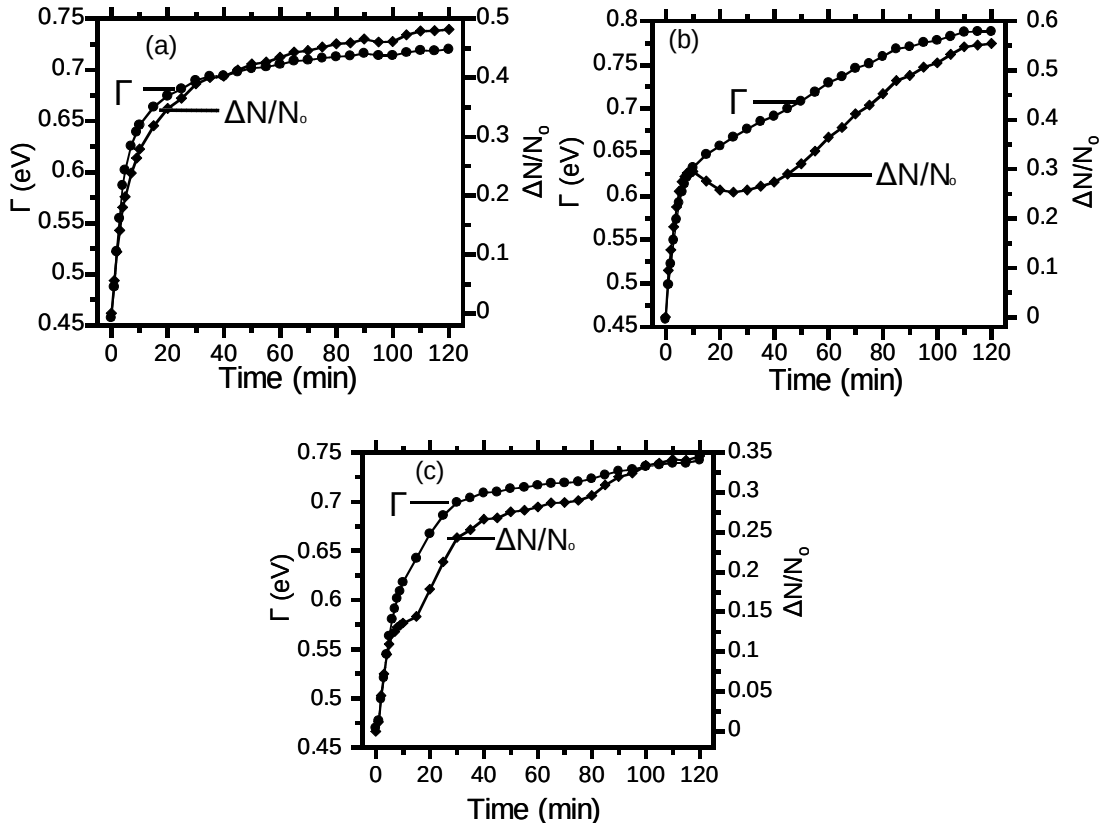

Figure 4.14: Comparison of damping factor and number of adsorbates in: (a) air; (b) nitrogen; and, (c) argon.

Chapter 5

Conclusions and Future Work

5.1 Conclusions

The present thesis work has developed a novel localized surface plasmon resonance (LSPR) chemical sensor on the basis of a unique sensing mechanism: adsorbate-induced damping of hybrid plasmon resonance. The sensor reports the width (damping factor) and intensity of the hybrid plasmon resonance associated with a monolayer of silver nanoparticles. These two parameters, continuously measured by optical extinction, are substituted in a theoretical relation (derived in the present work) to

quantify the number of electrons gained or lost (by the plasmon) due to the adsorbed molecules or atoms. The change in the number of free electrons precisely "counts" the number of adsorbates (which either donate or arrest free electrons by establishing metallic or covalent bonds with silver, respectively). The concentration level in turn can be computed from adsorption kinetics.

The plasmonic nanostructures are silver nanoparticle monolayers fabricated by electroless reduction of Ag^+ on silicon thin films. The silicon film not only serves as a reduction agent, but it also anchors the nanoparticles by Coulombic attraction due to opposite charging between silver and silicon. Further, the repulsion between the particles prevents aggregation despite a few nm of interparticle separation. As a result, strong and well-resolved hybrid plasmon modes develop.

It is found that a short (e.g., 1 min) annealing step at 300 ºC reduces the hybrid plasmon damping by close to a factor of 2. This dramatic reduction in intrinsic damping leads to a substantial enhancement in sensitivity, since now the contribution of adsorbate-induced damping to total damping is more pronounced. Interestingly, the same annealing has weak impact on the damping of the regular dipolar plasmon resonance. As inferred from atomic force microscopy and optical extinction, the annealing accounts for an increase in average particle size and separation. As to the origin of damping reduction, light scattering measurements reveal that the radiative damping factor reduces to 35% of its original value. This significant reduction in radiative damping is ascribed to restructuring of the monolayer of particles. One may also expect that reduction in damping originates from elimination of electron scatterers, such as grain boundaries and twins, by thermal energy (and therefore reduction of non-radiative damping). However,

high resolution TEM does not provide any clear evidence for the reduction of such structural defects. Accordingly, the reduction of hybrid plasmon damping is attributed mainly to a decrease in radiative damping as a result of the aforementioned restructuring.

The sensor response has been explored using mercury as the detection agent. Mercury is a severe neurotoxin whose contamination level in the environment has been tripled over the last century. The kinetics of hybrid plasmon intensity, H, in response to mercury exposure is found to have 3 subsequent regimes. According to Equation 3.3, $H = C\frac{N_{eo} + \Delta N_e}{\Gamma}$, the following conclusions are drawn regarding these 3 regimes: 1) Decrease in H due to increasing adsorbate-induced damping. This regime is absent in LSPR demonstrations reported in the literature which employed regular dipolar plasmon resonance. This is probably because; in these demonstrations, the adsorbate-induced damping cannot be the dominant sensing mechanism due to too high of an intrinsic damping factor present already. Or, the adsorbate-induced damping cannot be the dominant mechanism for regular dipolar plasmon modes, as the associated damping factor per adsorbate is too low for these modes; 2) minimization of H, followed by its increase. In this regime, electron transfer, ΔN_e, finally becomes the dominant mechanism regulating the hybrid plasmon extinction intensity, H. This suggests that the adsorbate-induced damping increases sub-linearly with the number of adsorbates. Similar sensing regime is exhibited by regular dipolar LSPR as reported by others. 3) Saturation of H. Saturation occurs due to the occupation of all mercury- adsorption sites.

When the sensor is exposed to mercury in argon and nitrogen, the variation of number of adsorbates is found to consist of multiple Langmuir isotherms superposed. This behavior may result from dissimilar adsorption/desorption rates at different classes

of sites on the nanoparticle surface. It is likely that, these different adsorption/desorption sites are associated with facets of different crystal orientations on the nanoparticle. Interestingly, when nitrogen is the ambient gas, a negative Langmuir isotherm is resolved, indicative of electron loss. It is concluded that, a chemical reaction occurs including silver, nitrogen and mercury [50]. The capturing and localization of metal electrons in Ag-N or $Hg_{adsorbed}$-N covalent bonds accounts for a decrease in the total number of electrons, which contribute to the plasmon. With argon as the ambient gas, no isotherms characteristic of electron loss are observed.

5.2 Future work

The present study demonstrates a unique approach of monitoring the kinetics of atomic/molecular adsorption on silver nanoparticles. In particular, the technique allows the tracing of Langmuir isotherms. The approach, therefore, is promising for the monitoring of surface chemical reactions. An interesting surface reaction is the chemisorption of H_2S on silver, which involves $2Ag + H_2S \rightarrow Ag - S - H + H + Ag \rightarrow Ag_2S + H_2$. Work is already under progress by Kalkan and co-workers.

Surprisingly, deconvoluted mercury Langmuir isotherms are seen to initiate at different times. Presently, the Author has no solid explanation for this behavior. However this is anticipated to be due to sequential filling of different adsorbate sites in the order from high energy to low energy sites facilitated by surface diffusion. Future work should elucidate this interesting observation.

In addition, the chemical interaction of nitrogen gas with silver and mercury leading to a possible $Ag_xHg_yN_z$ complex is not clear yet. This point can be elucidated by conducting surface- enhanced Raman scattering (SERS) on the sensor substrates, which are SERS-active. SERS can probe the formation of Ag–N and Hg–N bonds on the nanoparticles.

The next step in sensor development is the calculation of concentration from the kinetics. The adsorption of impurities on silver nanoparticles obeys the Langmuir's adsorption equation: $\Delta N_{Hg}(t) = \frac{Ck_aN}{Ck_a + K_d}\left(1 - e^{-(K_a+K_d)t}\right)$, where N is the total number of adsorption sites. C is the concentration. $K_a = Ck_a$ and K_d are adsorption and desorption coefficients, respectively. As usual, ΔN_{Hg} is deduced from the peak intensity and width (damping) of the hybrid plasmon extinction.

By differentiating the Langmuir isotherm at $t = 0$, we get

$$\frac{d}{dt}\Delta N_{Hg}(0) = Ck_aN \tag{5.1}$$

Therefore, once k_aN is extracted from a single sensor calibration measurement, C can be computed from the slope of the Langmuir isotherm at $t = 0$ as suggested by Equation 5.1.

C can also be deduced from the saturation regime at which $N_{Hg}(\infty) = \frac{k_aCN}{k_aC + K_d} = N\frac{C}{C + K_d/k_a}$. Accordingly, C can be evaluated as:

$$C = \frac{N_{Hg}(\infty)(K_d/k_a)}{N - N_{Hg}(\infty)} \tag{5.2}$$

Here, the values of N and K_d/k_a can be determined by two sensor calibration

measurements.

Bibliography

[1] U. Kreibig and M. Vollmer, *Optical Properties of Metal Cluster*: Springer, New York, 1995.

[2] Y. Xia and N. J. Halas, "Shape-Controlled Synthesis and Surface Plasmonic Properties of Metallic Nanostructures," *MRS Bulletin,* vol. 30, pp. 338-348, 2005.

[3] S. Link and M. A. El-Sayed, "Optical properties and ultrafast dynamics of metallic nanocrystals," *Annu. Rev. Phys. Chem.*, vol. 54, pp. 331-366, 2003.

[4] S. Link and M. A. El-Sayed, "Shape and size dependence of radiative, non-radiative and photothermal properties of gold nanocrystals," *Int. Rev. Phys. Chem.*, vol. 19, pp. 409-453, 2000.

[5] L. M. Liz-Marzán, "Nanomaterials: formation and color," *materialstoday,* pp. 26-31, 2004.

[6] P. Mulvaney, "Not all that's gold does glitter," *MRS Bulletin,* vol. 26, pp. 1-6, 2001.

[7] A. Henglein and M. Giersig, "Optical and chemical observations on gold-mercury nanoparticles in aqueous solution," *J. phys. chem. B,* vol. 104, pp. 5056-5060, 2000.

[8] A. J. Haes, R. P. V. Duyne, S. Zou, and George C. Schatz, "Nanoscale Optical Biosensor: Short Range Distance Dependence of the Localized Surface Plasmon Resonance of Noble Metal Nanoparticles," *J. phys. chem. B,* vol. 108, pp. 6961 - 6968, 2004.

[9] A. J. Haes and R. P. V. Duyne, "A Nanoscale Optical Biosensor: Sensitivity and Selectivity of an Approach Based on the Localized Surface Plasmon Resonance Spectroscopy of Triangular Silver Nanoparticles," *J. Am. Chem. Soc.*, vol. 124, pp. 10596 - 10604, 2002.

[10] L. Katsikas, M. Gutie´rrez, and A. Henglein, "Bimetallic colloids: Silver and Mercury," *J. phys. chem,* vol. 100, pp. 11203-11206, 1996.

[11] P. Nordlander, C. Oubre, E. Prodan, K. Li, and M. I. Stockman, "Plasmon hybridization for nanoshell dimmers," *Nano Letters,* vol. 7, pp. 899-903, 2004.

[12] T. A. Morris, "Novel Spectroscopic Methods to Monitor Mercury Adsorption to Gold and Silver Surfaces." vol. Ph.D. : University of Alabama, 2003.

[13] M. J. Pitkethly, "Nanomaterials-the driving force," *Nanotoday,* pp. 20-29, 2003.

[14] P. Nordlander and E. Prodan, "Plasmon hybridization in nanoparticles near metallic surfaces," *Nano Letters,* vol. 4, pp. 2209-2213, Nov 2004.

[15] P. Nordlander, C. Oubre, E. Prodan, K. Li, and M. I. Stockman, "Plasmon hybridizaton in nanoparticle dimers," *Nano Letters,* vol. 4, pp. 899-903, May 2004.

[16] K. H. Su, Q. H. Wei, and X. Zhang, "Interparticle Coupling effects on plasmon resonances of nanogold particles," *Nano Letters,* vol. 3, pp. 1087-1090, 2003.

[17] E. Prodan, C. Radloff, N. J. Halas, and P. Nordlander, "A hybridization model for the plasmon response of complex nanostructures," *Science,* vol. 302, pp. 419-422, Oct 2003.

[18] A. K. Kalkan and S. J. Fonash, "Electroless synthesis of Ag nanoparticles on deposited Nanostructured Si films," *J. Phys. Chem. B,* vol. 109, pp. 20779-22785, 2005.

[19] "The mercury problems fast facts, publication is a part of Going Green: A resource kit for pollution prevention in Health care," in *Pub 2-01*. vol. 4.

[20] "Impact of Mercury on the Environment," *United Nations Environment programme-Global Mercury Assessment,* vol. 5

[21] L. Bertilsson and H. Y. Neujahr, "Methylation of mercury compounds by methylcobalamin," *Biochem.,* vol. 10, pp. 2805-2808, 1971 July 6 1971.

[22] P. K. Jain and M. A. El-Sayed, "Surface Plasmon Resonance Sensitivity of Metal Nanostructures: Physical Basis and Universal Scaling in Metal Nanoshells," *J. Phys. Chem. C,* vol. 111, pp. 17451 - 17454, 2007.

[23] E. Prodan and P. Nordlander, "Plasmon hybridization in spherical nanoparticles," *Journal of Chemical Physics,* vol. 120, pp. 5444-5454, Mar 2004.

[24] A. J. Haes, W. P. Hall, L. Chang, W. L. Klein, and R. P. V. Duyne, "A Localized

surface plasmon resonance biosensor: first steps toward an assay for Alzheimer's disease," *Nano Letters,* vol. 4, pp. 1029-1034, 2004.

[25] A. J. Haes and R. P. Van Duyne, "A nanoscale optical biosensor: sensitivity and selectivity of an approach based on the localized surface plasmon resonance spectroscopy of triangular silver nanoparticles," *J. Am. Chem. Soc.,* vol. 124, pp. 10596-10604, 2002.

[26] N. K. Grady, N. J. Halas, and P. Nordlander, "Influence of dielectric function properties on the optical response of plasmon resonant metallic nanoparticles," *Chemical Physics Letters,* vol. 399, pp. 167-171, Nov 2004.

[27] D. J. Maxwell, J. R. Taylor, and S. Nie, "Self- Assembled nanoparticle probes for recognition and detection of biomolecules," *J. Am. Chem. Soc.,* vol. 124, pp. 9606-9612, 2002.

[28] A. D. McFarland and R. P. V. Duyne, "Single silver nanoparticles as real time optical sensors with zeptomole sensitivity," *Nano Letters,* vol. 3, pp. 1057-1062, 2003.

[29] Y. Iwasaki, T. Horiuchi, and O. Niwa, "Detection of electrochemical enzymatic reactions by surface plasmon resonance measurement," *Anal. Chem.,* vol. 73, pp. 1595-1598, 2001.

[30] Z. Jing, Z. Xiaoyu, Y. C. Ranjit, H. A. J, and R. P. Van Duyne, "Localized surface plasmon resonance biosensors," *Nanomedicine,* vol. 1, pp. 219-228, 2006.

[31] T. Okamoto, I. Yamaguchi, and T. Kobayashi, "Local plasmon sensor with gold colloidal monolayers deposited upon glass substrates," *Opt. lett,* vol. 25, pp. 372-374, 2000.

[32] J. J. Mock, D. R. Smith, and S. Schultz, "Local refractive index dependence of plasmon resonance spectra from individual nanoparticles," *Nano Letters,* vol. 3, pp. 485-490, 2003.

[33] M. A. Butler, A. J. Ricco, and R. J. Baughman, "Hg adsorption on optically thin Au films," *J. appl. phys,* vol. 67, pp. 4320-4326, 1990.

[34] T. Morris, H. Copeland, E. McLinden, S. Wilson, and G. Szulczewski, "The effect of Mercury adsorption on the optical response of selected gold and silver nanoparticles," *Langmuir,* vol. 18, pp. 7261-7264, 2002.

[35] T. Morris, K. Kloepper, S. Wilson, and G. Szulczewski, "A Spectroscopic study

of mercury vapor Adsorption on gold nanoparticle films," *J. Col. Int. Sci*, vol. 254, pp. 49-55, 2002.

[36] T. Morris and G. Szulczewski, "A spectroscopic ellipsometry, surface plasmon resonance and X-ray photoelectron spectroscopy study of Hg adsorption on gold surfaces," *Langmuir*, vol. 18, pp. 2260-2264, 2002.

[37] R. P. Bajpai, H. Kita, and K. Azuma, "Adsorption of water on Au and mercury on Au, Mo, and Re- measurements of changes in work function," *Jpn. J. Appl. Phys*, vol. 15, p. 2083, 1976.

[38] A. K. Kalkan, "Mercury detection with Ag nanoparticles reduced on Si thin films," *Mater. Res. Soc. Symp. Proc.*, vol. 1010, p. 09, 2007.

[39] U. Kreibig and C. V. Fragstein, "The limitation of electron mean free path in small silver particles," *Z. Phys.*, vol. 224, pp. 307-323, 1969.

[40] B. N. J. Perrson, "Polarizability of small spherical metal nanoparticles: influence of the matrix environment," *Surf. Sci*, vol. 281, pp. 153-162, 1993.

[41] H. Hövel, S. Fritz, A. Hilger, M. Vollmer, and U. Kreibig, "Width of cluster plasmon resonances: Bulk dielectric functions and chemical interface damping," *Phys. Rev. B*, vol. 48, pp. 18178-18188, 1993.

[42] Y. Z. Wang and O. O. Awadelkarim, "Polycrystalline silicon thin films formed by metal-induced solid phase crystallization of amorphous silicon," *J. Vac. Sci. & Tech.*, vol. 16, pp. 3352-3358, 1998.

[43] R. H. Dreisbach, *Handbook of poisoning: diagnosis and treatment*: Lange Medical Publications, 1959.

[44] T. G. Winter, "The evaporation of a drop of mercury," *J. Am. Phys.*, vol. 71, pp. 783-786, 2003.

[45] C. Dahmen, B. Schmidt, and G. v. Plessen, "Radiation damping in metal nanoparticle pairs," *Nano Letters*, vol. 7, pp. 318-322, 2007.

[46] S. Karumuri and A. K. Kalkan, "Damping of Hybrid surface plasmon modes in Ag Nanoparticles: application to vapor sensing," in *Minerals, Metals & Materials Society Annual Meeting*, New Orleans, LA, 2008.

[47] R. Imbihl, R. J. Behm, and G. Ertl, "The Structure of atomic nitrogen adsorbed on Fe(100)," *Surface. Science*, vol. 123, pp. 129-140, 1982.

[48] G. Ertl, S. B. Lee, and M. Weiss, "Kinetics of nitrogen adsorption on Fe(ll1)," *Surface Science,* vol. 114, pp. 515-526, 1982.

[49] F. Bozso, G. Ertl, M. Grunze, and M. Weiss, "Interaction of Nitrogen with Iron Surfaces I. Fe(100) and Fe(111)," *Journal of Catalysis* vol. 49, pp. 18-41, 1977.

[50] Feedback given by Dr. Barry K. Lavine.

VITA

Sriharsha Karumuri

Candidate for the Degree of

Master of Science in Mechanical Engineering

Thesis: Hybrid Surface Plasmon Damping Chemical Sensor

Major Field: Mechanical Engineering

Biographical:

Personal Data:	Born on June 5, 1985 in Anakapalli, Andhra Pradesh, India.
Education:	Completed Bachelor of Engineering degree in Mechanical Engineering from Andhra University in May 2006
Education:	Completed the requirements for the Master of Science in Mechanical Engineering at Oklahoma State University, Stillwater, Oklahoma in May, 2009.
Experience:	Worked as a Research Assistant at Oklahoma State University in Functional Nanomaterials Laboratory.

_____

Name: Sriharsha Karumuri Date of Degree: May, 2009

Institution: Oklahoma State University Location: Stillwater, Oklahoma.

Title of Study: HYBRID SURFACE PLASMON DAMPING CHEMICAL SENSOR

Pages in Study: 61 Candidate for the Degree of Master of Science

Major Field: Mechanical Engineering

Scope and Method of Study:
The present thesis work demonstrates a novel localized surface plasmon resonance (LSPR) chemical sensor on the basis of a unique sensing mechanism: adsorbate-induced damping of hybrid plasmon resonance. The sensor reports the width (damping factor) and intensity of the hybrid plasmon resonance associated with a monolayer of silver nanoparticles. These two parameters, continuously measured by optical extinction, are substituted in a theoretical relation (derived in the present work) to quantify the number of electrons gained or lost (by the plasmon) due to the adsorbed molecules or atoms. The change in the number of free electrons precisely equals the number of adsorbates. The plasmonic nanostructures are silver nanoparticle monolayers fabricated by electroless reduction of Ag^{+} on Si thin films. The nanoparticle monolayers are exposed to a short annealing step to reduce the hybrid plasmon damping by close to a factor of 2. This dramatic reduction in intrinsic damping leads to a substantial enhancement in sensitivity, since now the contribution of adsorbate-induced damping to total damping is more pronounced.

Findings and Conclusions:
The sensor response has been explored using mercury as the detection agent. Detection of ppb levels of mercury has been accomplished. Further, the sensor is found to be capable of resolving multiple Hg Langmuir adsorption isotherms. These different adsorption isotherms are likely to be associated with different crystalline directions (i.e., facets) on the nanoparticle surfaces. Interestingly, the isotherms are found to start at different times. Also surprising is that, sensor response indicates dissociation of N_2 on Ag nanoparticles and a chemical reaction between Ag, N, and Hg. As to the origin of damping reduction by the aforementioned annealing step, light scattering measurements reveal that the radiative damping factor reduces to 35% of its original value.

ADVISER'S APPROVAL: Dr. A. Kaan. Kalkan